



NTNU – Trondheim
Norwegian University of
Science and Technology

Effects of Heat Treatment on Microstructure, Strength and Hardness of F22 Steel

Trond Arne Hassel

Materials Science and Engineering

Submission date: June 2013

Supervisor: Jan Ketil Solberg, IMTE

Co-supervisor: Per Thomas Moe, FMC Technologies

Norwegian University of Science and Technology
Department of Materials Science and Engineering

Preface

The work presented in this master's thesis is the result of a collaboration between FMC Technologies at Kongsberg and Department of Materials Science and Engineering at NTNU. It was initiated by FMC Technologies in order to assess the suitability of forge welding for production of riser systems.

I would like to thank my supervisor, Professor Jan Ketil Solberg for his patience when I have come knocking at his door with questions. His knowledge of microstructures and effects from different heat treatments has been most valuable. I have appreciated our discussions regarding my results.

I would also like to thank my co-supervisor, Professor II Per Thomas Moe at FMC Technologies Kongsberg. His help has been valuable in providing an overview and understanding the environment in which risers operate. In addition, he has been helpful in acquiring relevant information, both regarding riser systems and forge welding.

Welding Engineer Svein Bratterud at FMC Technologies Kongsberg has been helpful providing information regarding mechanical requirements and the testing procedures performed when qualifying welds in the production of riser systems.

In addition, a thanks should be directed to Principal Engineer Pål Skaret for his help with numerous tensile tests.

Abstract

In offshore oil exploitation, the riser is an important component, linking the installations on the seabed to the surface installations. This master's thesis has looked at the possibility of implementing forge welding in riser production. The focus has been on mechanical properties in riser steel subjected to the thermal effects from forge welding. Continuing the findings from the forge welding investigations, relations between strength and hardness has been established.

Thermal simulation of forge welding was carried out. The material was then tempered at 650°C for respectively 1, 3 and 6 hours. Hardness profiles were measured across the HAZ, as well as tensile testing of the base material. Tempering for 1 hour produced HAZ hardness below 275 HV, but 6 hours of tempering was necessary to bring the hardness below 250 HV. Tensile testing confirmed suspicions from prior work about provided material not fulfilling the requirements for yield and tensile strength.

The establishment of a strength-hardness relationship started with microstructural investigations. These included light microscopy, microhardness measurements, SEM imaging and EDS analysis to determine the effect of prolonged tempering, as well as to identify the microstructures formed by various heat treatments. It was found that as-quenched material contained a martensitic structure with no visible carbides. Material tempered for a short period of time contained lath shaped cementite, while alloy carbides of chromium and molybdenum formed in material subjected to prolonged tempering. Material subjected to controlled cooling or isothermal heat treatment at 600°C and 700°C formed ferrite-pearlite structures. However, instead of lamellar pearlite, a form of degenerate pearlite was observed in two out of three samples.

A comparison of different tempering temperatures was done by using the Hollomon-Jaffe parameter to determine tempering effect. This study proved the Hollomon-Jaffe relationship valid for tempering of F22 steel, since the same hardness reduction was achieved for tempering cycles with equal tempering parameter. The comparison also accentuated the strong dependence of temperature on achieved tempering effect.

Tensile testing and corresponding hardness measurements were used for determining linear regressions between strength and hardness for F22 steel. Regressions for both yield- and tensile strength were found. When compared to already existing relations between strength and hardness, the new models proved more accurate for the F22 steel. However, approximating tensile strength proved more precise than approximating yield strength due to plastic deformation and work hardening.

Sammendrag

Risere er en viktig del av offshore olje- og gassutvinning som forbinder installasjoner på havbunnen med overflateinstallasjoner. Denne masteroppgaven har sett på muligheten for å benytte smisveising i produksjon av risere. Fokus har vært på mekaniske egenskaper i stål utsatt for de termiske effektene fra smisveising. For å bygge videre på resultatene fra smisveiseundersøkelsene har sammenhenger mellom styrke og hardhet blitt etablert.

Termisk sveisesimulering av F22-stål har blitt utført. Materialet ble deretter anløpt ved 650°C i 1, 3 og 6 timer. Hardhetsprofiler ble målt på tvers av varmpåvirket sone, i tillegg til strekkprøving av materialet. Anløping i 1 time gav hardhetsverdier under 275 HV, men hele 6 timer måtte til for å få hardheten under 250 HV. Strekkprøving bekreftet mistankene fra tidligere undersøkelser om at det leverte materialet ikke oppfylte kravspesifikasjonene med hensyn på flytespenning og strekkfasthet.

Etableringen av en relasjon mellom styrke og hardhet startet med mikrostrukturundersøkelser. Lysmikroskopi, mikrohardhetsmålinger, SEM-avbildning og EDS-undersøkelser ble utført for å bestemme virkningen av langvarig anløping i tillegg til å identifisere mikrostrukturer dannet under ulike varmebehandlinger. Undersøkelsene viste at bråkjølt material ikke inneholdt synlige karbider og hadde en ren martensittstruktur. Material anløpt i kort tid inneholdt cementittnåler, mens material anløpt over lengre tid inneholdt legeringskarbider av krom og molybden. Material som hadde blitt avkjølt kontrollert fra herdetemperatur eller blitt isotermt varmebehandlet ved 600°C eller 700°C hadde dannet ulike ferritt-perlitt-strukturer. I to av tre prøver med ferritt-perlitt-struktur hadde en degenerert perlitt blitt dannet i stedet for lamellær perlitt.

En sammenlikning av ulike anløpningstemperaturer ble gjennomført ved å benytte Hollomon-Jaffe parameteren for å bestemme anløpingseffekt. Dette bekreftet at Hollomon-Jaffe-sammenhengen er gyldig for anløping av F22-stål, siden anløpingsforløp med lik anløpingsparameter gav samme hardhetsreduksjon. Sammenlikningen fremhevet også temperaturens store innvirkning på anløpingseffekten.

Strekkprøving og tilhørende hardhetsmålinger ble benyttet som grunnlag for å bestemme lineære regresjoner mellom styrke og hardhet i F22-stål. Regresjoner for både flytespenning og strekkfasthet ble bestemt. Den nye modellen var mer presis for F22-stål, sammenliknet med eksisterende styrke-hardhetsrelasjoner. Å bestemme strekkfasthet på bakgrunn av hardhetsmålinger gav bedre presisjon enn flytespenning på grunn av plastisk deformasjon og arbeidsharding.

Contents

Preface	i
Abstract	iii
Sammendrag	v
1. Introduction	1
2. Theory	3
2.1. Ferrite-pearlite	3
2.2. Bainite	5
2.3. Martensite	6
2.4. IT- and CCT-diagrams	6
2.5. Tempering of martensite	7
2.6. Effect of alloying elements	11
2.7. Production and processing of F22 steel	12
2.8. Forge welding	13
2.9. Previous work on strength-hardness relations	14
3. Experimental	17
3.1. Material	17
3.2. Heat treatment	18
3.2.1. Weld simulation	18
3.2.2. Tempering	20
3.2.3. QT-heat treatment	20
3.3. Vickers hardness measurements	22
3.3.1. Weld hardness profiles	22
3.3.2. Hardness of tensile specimens	23
3.4. Tensile testing	24
3.5. Data analysis and statistics	26
3.6. Metallographic preparation	26
3.7. Microscopy and microhardness	27
3.8. SEM investigation	27
4. Results	29
4.1. Forge welding investigations	29
4.1.1. Hardness profiles	29
4.1.2. Hardness development during tempering	32
4.1.3. Tensile testing	32
4.2. Strength-hardness relation	35
4.2.1. Metallographic investigation	35
4.2.2. SEM-investigation	40
4.2.3. Validity of the Hollomon-Jaffe relationship for F22 steel	50
4.2.4. Strength-hardness relations	54
4.2.5. Comparison with previous strength-hardness relations	57

5. Discussion	59
5.1. Weld simulation investigations	59
5.1.1. Weld hardness profiles	59
5.1.2. Hardness development	60
5.1.3. Tensile testing	60
5.2. Strength-hardness relationship	62
5.2.1. Metallographic and SEM examination	62
5.2.2. Validity of the Hollomon-Jaffe relationship for F22 steel . . .	64
5.2.3. Strength-hardness relations	65
5.2.4. Comparison with previous strength-hardness relations	65
6. Conclusion	67
7. Further work	69
Appendices	75

1. Introduction

Riser pipes are important components in offshore oil exploitation. They connect the rig or vessel to installations on the seabed, see Figure 1 for illustration. The riser pipes are equipped with mechanical connectors welded to the ends of each pipe. The connectors make it possible to quickly assemble a riser string. This joining method avoids the possibility for defects from welding of pipes offshore, as well as avoiding the risk of fire and explosion when welding on-board offshore installations [1, pp. 381–385].

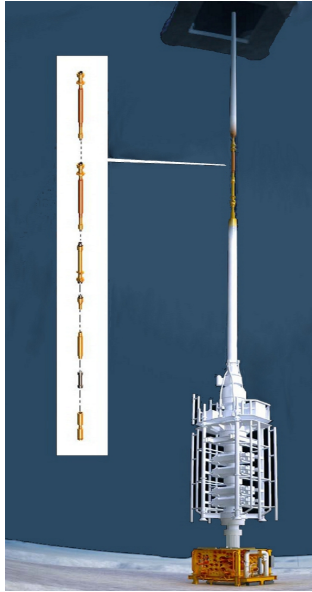


Figure 1: *Illustration of a riser system extending from the rig down to a BOP. The exploded drawing next to the pipe shows mechanical connectors welded to the ends of each pipe segment. Modified from a FMC illustration [2].*

Fusion welding is the traditional welding technique used in most joining applications. It relies on placing a filler metal in the weld groove, which is heated until it melts. The necessity of multipass welds makes fusion welding a slow and labour intensive welding procedure. Forge welding, on the other hand, is a technique for joining of metals at temperatures below their melting temperature. This technique relies on heating and pressure in order to join the metal surfaces. Forge welding can be performed fast and with a high degree of automation, enabling the production of high quality joints within a matter of minutes. In addition, forge welds tend to exhibit good mechanical properties due to low heat input during joining [3].

Over the past years, several projects and master's theses [4–11], together with two ongoing doctoral works, have studied the metallurgical aspects regarding forge welding of steels. The first project started in 2008 as a collaboration between AMR

Engineering and NTNU, Department of Materials Science and Engineering. Since then, both ferrite-pearlite and QT steel grades have been investigated. Prior to this master's project, the following steels have been examined: API 5CT J55 [4, 5, 8], K55 [7], L80 [4, 6, 7], L80SS [7] and C90 [11], as well as API 5L X65 [9], X80 [10] and F22 [12].

FMC Technologies at Kongsberg is the industrial partner in this thesis. Their interest is to assess the suitability of forge welding for production of offshore riser systems. The scope of this master's work is to continue the examinations started by the present author [12] by investigating the effects from heat treatment of F22 steel. The findings in the previous work investigating F22 steel [12], gave reason to question the strength of the supplied material, regardless of heat treatment. It has therefore been decided that a more precise correlation between strength and hardness could prove more useful than further investigations regarding thermal simulation of forge welding. In order to complement previous findings, the investigations have been concentrated as to partly overlapping fields of study:

1. A short investigation to confirm whether the base material complies with the material certificate or not, and a series of weld simulations followed by tempering at 650°C and mechanical testing to compare these results with the findings and predictions stated by the present author [12].
2. The establishment of a relation between strength and hardness for F22 steel.

The forge welding investigations will try to satisfy requirements for mechanical properties according to ISO 13628-7 and the internal FMC standard, M20717, after thermal simulation of forge welding. In this master's thesis, the experimental procedures will focus on achieving HAZ hardness below 250 HV and 275 HV, which are the requirements for hardness in fusion line in respectively root and cap regions of the weld. The other main focus in the forge welding investigations will be strength, where the minimum requirements for yield and tensile strength are respectively 586 MPa and 689 MPa. The full list of requirements is shown in Appendix A.1, p. 75.

In general, a linear approximation between hardness and yield strength can be assumed to be valid. Such an approximation has been provided by Pavlina and Van Tyne [13], but their work is of more general character and is a rough estimate for several different steel qualities and microstructures. Their correlations are therefore imprecise and uncertain when applied on quenched and tempered F22 steel. Earlier work on strength and hardness relations include Tabor [14], Cahoon et al. [15, 16], Marcinkowski et al. [17] and Speich and Warlimont [18]. They have all performed investigations relating strength and hardness, but common for all these is that their relations are of a more general type. Most of these relations are crude, like $R_{p0.2} = \frac{HV}{3}$ [15], which is valid for severely cold worked materials. Other prior relations between strength and hardness require knowledge of the strain hardening exponent, n , for the specific steel. Therefore, this thesis will try to establish a more reliable relation between strength and hardness for F22 steel, based entirely on bulk hardness.

2. Theory

This chapter will attempt to build a theoretical background for this thesis. First, theory surrounding some microstructures in steel will be presented, followed by a part presenting steel production and processing. Finally, the last section will introduce the theory behind forge welding.

Several of the sources used for the theory are old, but still valid, and considered necessary to provide the background needed for a full understanding of the processes taking place when heat treating F22 steel. There is little scientific work available on F22 steel in quenched and tempered state. However, there have been some investigations regarding 2.25Cr-1Mo steel for pressure vessels, heat exchangers and boilers, but these usually focus on steels with ferrite-pearlite structure for elevated temperature service [19]. It has therefore been considered useful to look at older sources to gain a wider understanding of the microstructural changes taking place during heat treatment of steel.

2.1. Ferrite-pearlite

Ferrite-pearlite is the equilibrium microstructure obtained during slow cooling of steels containing up to 0.8 wt% carbon. Growth of ferrite starts at the austenite grain boundaries (GB), and with lowering α/γ transformation temperatures, four different morphologies of ferrite can be identified, as presented by Dubé [20, pp. 42–44]:

1. Grain boundary allotriomorphs: Grow along austenite GB, stretching into both the surrounding austenite grains. Random orientation with one austenite grain, more coherent orientation with the other grain. Can therefore be faceted on one side and curved on the other.
2. Widmanstätten ferrite plates or laths: Nucleate at austenite GB, and grow along well-defined austenite planes. Will not cross austenite GB. Primary Widmanstätten ferrite forms directly on austenite GB, while secondary Widmanstätten ferrite grows from other allotriomorphs of ferrite.
3. Intragranular idiomorphs: Equi-axed ferrite that nucleate inside austenite grains, often on non-metallic inclusions. Will have some crystallographic facets.
4. Intragranular plates: Similar to Widmanstätten plates, but nucleate inside austenite grains without being in contact with GB.

Usually, combinations of the different morphologies are present. An example of this is growth of ferrite during continuous cooling, where formation of grain boundary allotriomorph ferrite comes first, followed by growth of secondary Widmanstätten ferrite from the grain boundary allotriomorph, and finally, the formation of intragranular idiomorphs or plates. This effect is illustrated in Figure 2, where different

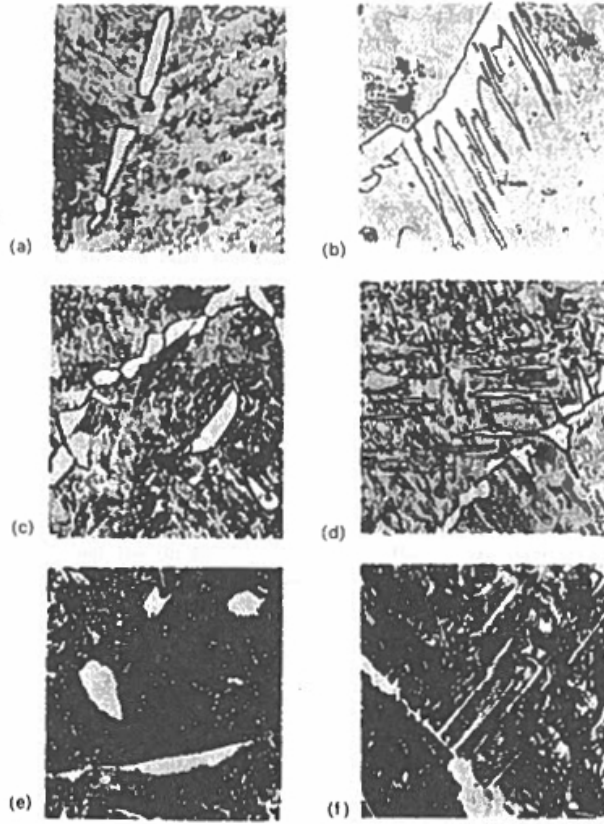


Figure 2: *Different morphologies in pro-eutectoid ferrite and hyper-eutectoid cementite (Courtesy of R.A. Ricks) [20, p. 43] :*

- a) 0.34 wt% C, 12 minutes at 790° C. GB allotriomorphs of ferrite.
- b) 0.34 wt% C, 15 minutes at 725° C. Widmanstätten ferrite growing from GB ferrite.
- c) 0.34 wt% C, 12 minutes at 790° C. GB allotriomorphs and intragranular idiomorphs of ferrite. d) 0.34 wt% C, 15 minutes at 725° C. Intragranular Widmanstätten ferrite plates. e) 1.2 wt% C, 10 minutes at 730° C. GB allotriomorphs and intragranular idiomorphs of cementite.
- f) 1.2 wt% C, 10 minutes at 730° C. Widmanstätten cementite.

morphologies are shown together in the same picture.

Diffusion during growth of ferrite leads to accumulation of carbon in the austenite. This eventually results in the formation of pearlite. A microstructure which forms through the eutectoid reaction, as shown in Equation 1.



Pearlite is a lamellar structure consisting of parallel lamellae of cementite (θ -carbide) and ferrite layered in a sandwich structure. The formation of pearlite enables continued growth of the equilibrium phases while minimizing diffusion distance during growth. Because of its high strength, pearlite is an important constituent in steels [20, pp. 53–54]. However, pearlite is not favoured in offshore engineering because of its low impact toughness.

Due to kinetics, the growth temperature will determine the thickness of the pearlitic lamellae. Low cooling rates or high transformation temperatures will result in coarse lamellae, while high cooling rates or low transformation temperature will produce fine lamellae due to lower diffusivity [21].

Obtaining a ferrite/pearlite microstructure is dependent on slow cooling. This is shown in Figure 4, where it can be seen that only very slow cooling will produce a ferrite-pearlite structure in F22 steel.

2.2. Bainite

Bainite is a microstructure formed in the intermediate between ferrite-pearlite and martensite. This is shown in Figure 4, where both the IT- and CCT-diagram show the bainite nose. A bainitic microstructure can be obtained by a cooling rate too low to produce pure martensite, while still too high to produce ferrite-pearlite. Bainite can also be produced through isothermal heat treatment.

The bainite microstructure consists of ferrite plates or laths. These are separated by residual phases like retained austenite, martensite or cementite. The bainitic plates are called subunits, which grow in clusters called sheaves, see Figure 3. Within each sheaf, the subunits are separated by low-misorientation grain boundaries or residual phases. Sheaves are also referred to as “packets” of bainite [22, p. 129].

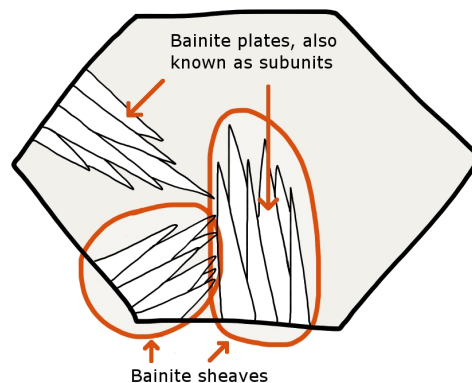


Figure 3: *Sketch illustrating the structures found in bainite. The difference between plates or subunits and sheaves of bainite is shown.*

2.3. Martensite

Martensite is a hard and brittle phase that forms when austenite is cooled too fast to form bainite. Martensite is obtained with cooling rates high enough to avoid the bainite nose, see Figure 4. The martensite reaction is often referred to as a diffusionless, shear transformation, which induces a shape change in the transformed region. The transformation is dependent on maintaining a high degree of coherency in the transformation interface. This results in an invariant-line strain, where one line in the transformation interface is unrotated and undistorted. The diffusionless nature of the martensite reaction leaves carbon trapped in interstitial positions, which introduce lattice strains. In order to reduce strain energy from the surroundings, martensite forms as thin plates or laths [20, pp. 95–106].

The martensite reaction is athermal. This means that the fraction transformed is only dependent on the undercooling below the martensite-start temperature (M_s). Carbon, having been in solid solution in the austenite, will remain in solid solution in the martensite as well due to the high cooling rate and fast transformation [20, pp. 95–96].

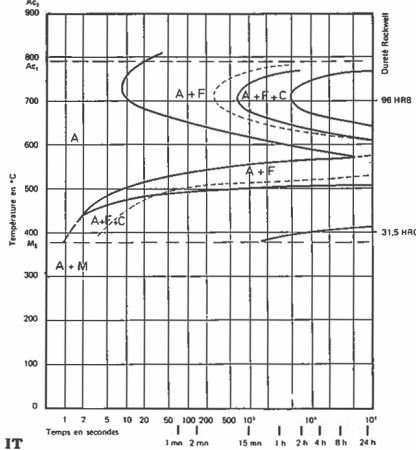
Austenite has an fcc structure. The martensite that forms from it can have various crystal structures, dependent on the content of alloying elements. Both bcc, bct and hcp structures can be found in martensite [23]. The martensitic microstructure consists of laths in low- or medium-carbon steels, while the martensite forms as plates in high-carbon steels. The laths formed in low-carbon steels are fine, form at the grain boundaries and can stretch across an entire former austenite grain. The laths group together in sheaves or packets, like bainite (Figure 3). Each lath has a substructure consisting of a high density of dislocations arranged in cells, where one lath contains many cells. The cells have an average width of 2500 Å, and typical dislocation densities are estimated to be between 0.3 and $0.9 \cdot 10^{12}$ cm/cm³ [23].

2.4. IT- and CCT-diagrams

IT- and CCT-diagrams provide a visualised connection between thermodynamics and kinetics. They show which phases will form during heat treatment at given time and temperature/cooling rate. Figure 4 shows both IT- and CCT-diagrams for a steel with almost the same composition as the F22 steel investigated in this study, see Section 3.1, Table 1 (p. 17) for composition of F22.

10 CD 9-10 Steel

Composition: 0.15% C - 0.36% Mn - 0.44% Si - 0.020% S - 0.022% P - 0.09% Ni - 2.24% Cr - 0.85% Mo - 0.23% Cu - 0.097% Al - 0.01% Ti Grain size: 10 Austenitized at 975°C (1700°F) for 30 min



Composition: 0.15% C - 0.36% Mn - 0.44% Si - 0.022% S - 0.020% P - 0.09% Ni - 2.24% Cr - 0.85% Mo - 0.23% Cu - 0.097% Al - 0.01% Ti Grain size: 10 Austenitized at 925°C (1700°F) for 30 min

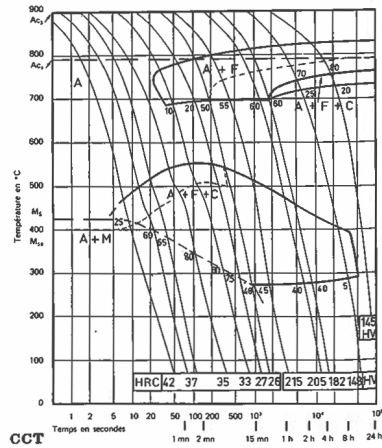


Figure 4: *IT- and CCT-diagram for a steel with closely matching composition to that of the F22 steel investigated in this study [24, p. 186].*

2.5. Tempering of martensite

Martensite is a hard and brittle structure, but in its tempered state, it provides one of the best combinations of strength and toughness obtainable in low carbon steels. This makes tempering of martensite one of the most important heat treatments in modern steelmaking.

Different combinations of time and temperature can give the desired mechanical properties during tempering, but, in general, temperature will have the highest impact on tempering effect [25]. The tempering process can be divided into four stages, where temperature is the determining factor [20, pp.184–189]:

- Stage 1: From room temperature to 250°C. Precipitation of ϵ -carbide. Partial loss of tetragonality. Steels with less than 0.25 wt% C are not likely to precipitate ϵ -carbide.
- Stage 2: 200°C to 300°C. Decomposition of retained austenite to bainitic ferrite and cementite.
- Stage 3: 200°C to 350°C. ϵ -carbide replaced by cementite. Martensite loses tetragonality and the matrix essentially turns into ferrite.
- Stage 4: 300°C to 700°C. Coarsening and spheroidization of cementite. Recrystallization causes formation of ferrite at temperatures close to 700°C.

Initial hardness reduction during tempering is often accredited to segregation and

precipitation of carbon and loss of tetragonality, followed by annihilation of dislocations above 300°C, as shown in Figure 5. Decomposition of potential retained austenite will also take place, but will not contribute to softening, especially not for a low carbon steel like F22, where the amount of retained austenite is negligible [26]. Prolonged tempering will often lead to an Ostwald ripening of cementite particles, as observed by Speich [27] as well as by Caron and Krauss [28]. Common for all these processes is that they will reduce strength, while the toughness of the steel is increased.

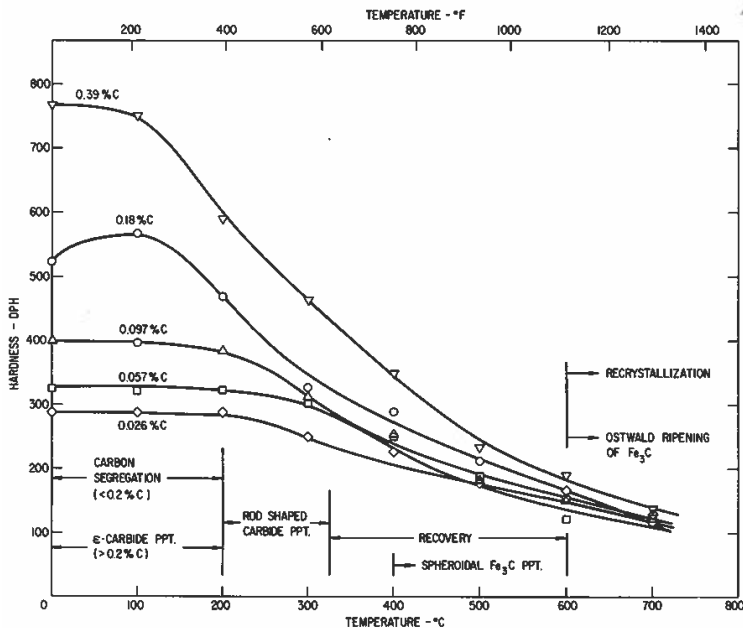


Figure 5: Hardness change in iron-carbon martensite tempered for 1 hour as a function of tempering temperature [27].

Most theory and studies considering tempering of martensite focus on variations in temperature, applying the traditional tempering time of 1 hour. This is illustrated in Figure 5, where the change in hardness as a function of temperature is shown for steels with varying carbon content having been tempered for 1 hour [27].

One article that deviates from the traditional fixed tempering time is “An Investigation of the Validity of Certain Tempering Parameters” by Murphy and Woodhead [29]. Their work focuses on comparing different approaches to the effect of tempering, and they found that the Hollomon-Jaffe relation (Equation 2) is the most successful in covering a wide range of hardness changes. A graph presenting some of Murphy and Woodhead’s results is shown in Figure 6. Note how the curves exhibit a fairly similar initial hardness reduction, and that the temperature seem to be a determining factor for the final hardness.

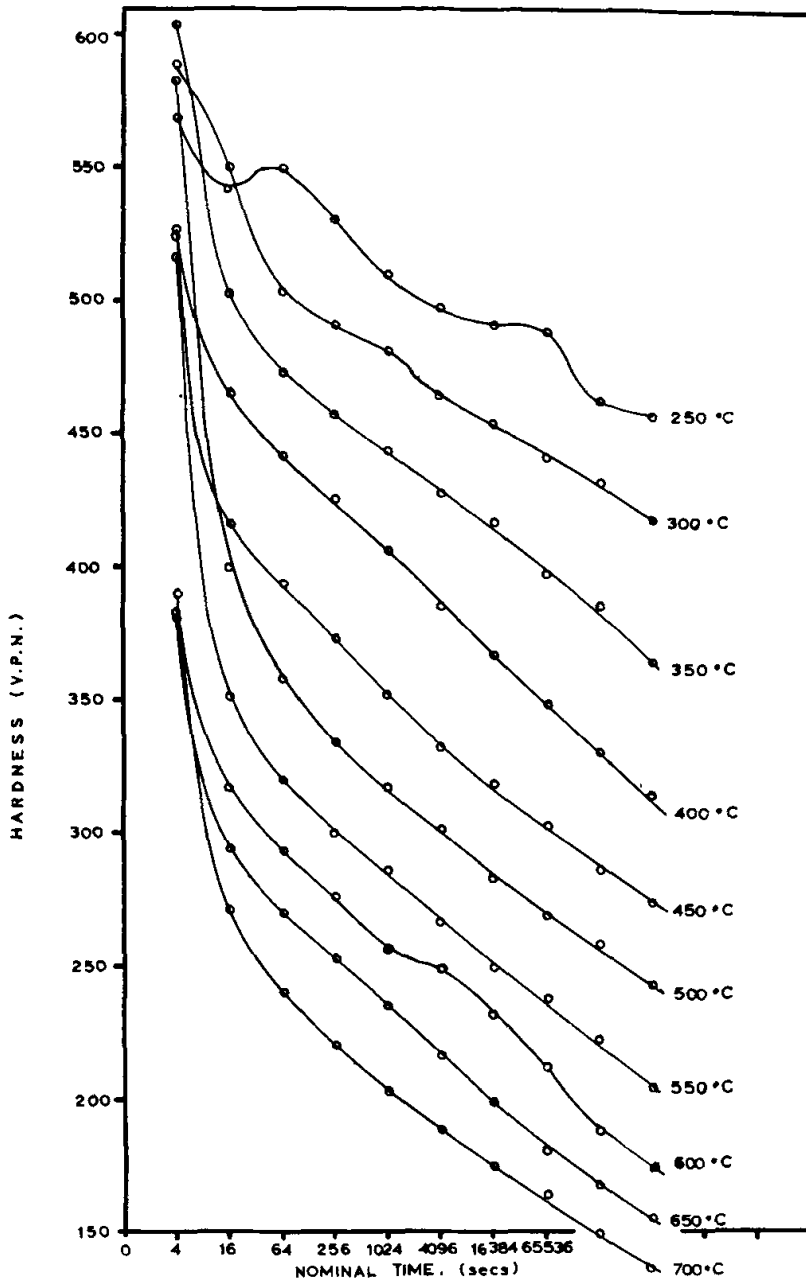


Figure 6: *Hardness development during tempering at different temperatures. A summary of some of the results of Murphy and Woodhead. Note how the shape of the curves contain the same initial hardness reduction, while the final hardness to a large extent is determined by the tempering temperature [29].*

Carbides will precipitate during tempering. In addition to loss of potential tetragonality and relief of lattice stresses, the precipitated carbides can act as pinning sites during recovery of martensite laths. Finer cementite particles or elongated interlath cementite formed during non-isothermal tempering have been reported to retard lath boundary migration [26]. This effect led to less hardness reduction when compared to isothermal tempering, where the cementite particles were found to be fewer and coarser [26].

Auto-tempering is an important factor when considering the mechanical properties in martensitic steels. Most low carbon steels have a relatively high M_s , resulting in auto-tempering of the martensite that forms first while the steel cools to ambient temperature. During cooling, the carbon segregates to lattice defects [23]. According to Speich [27], almost 90 % of the carbon segregates to lattice defects during quenching of steels containing less than 0.2 % carbon.

The Hollomon-Jaffe parameter is an empirical relation developed by J.H. Hollomon and L.D. Jaffe in 1945 [25]. It gives a relationship for tempering of martensitic steels, which correlates time, temperature and achieved tempering effect (measured as hardness reduction):

$$z = T(c + \log t) \quad (2)$$

Where z is the Hollomon-Jaffe parameter, T is the temperature in Kelvin, c is a constant dependent of the alloy content of the steel ($c \approx 20$), and t is the time in hours. Combinations giving the same parameter, z , will result in equal hardness reduction [25]. According to the investigations performed by Hollomon and Jaffe, the constant, c , is expected to be 20.6 for steels containing 0.12 wt% carbon, but this estimate is based on interpolation of the results obtained by Hollomon and Jaffe, since the lowest carbon content in their investigations was 0.31 wt% [25].

The validity of the Hollomon-Jaffe parameter has been proven time and again since it was published in 1945. As mentioned above, Murphy and Woodhead found that it was the most effective parameter when applied over a wide range of hardness changes. Semiatin et al. [30] also found that the Hollomon-Jaffe parameter was a good measure of tempering effect, even for short, isothermal tempering treatments lasting only a few seconds.

Secondary hardening is an effect to take into consideration when tempering steels containing chromium, molybdenum, titanium, tungsten or vanadium. These elements are strong carbide formers, and will precipitate as alloy carbides in preference to cementite at temperatures from 500–600°C. Due to their slow, substitutional diffusion, these elements will in most practical applications form fine, dispersed carbides. Aided by higher thermodynamic stability, the dispersed alloy carbides will replace coarser cementite particles, and because of their “sluggish” diffusion, they will remain small and dispersed even at elevated temperatures [20, pp. 195–197].

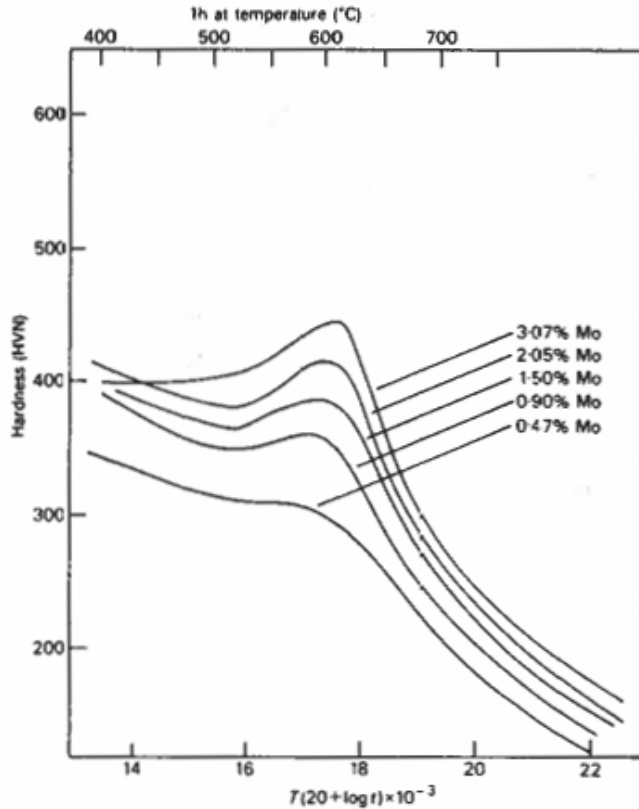


Figure 7: *The effect of molybdenum on the tempering of quenched 0.1 wt% C steel. Increased addition leads to increased secondary hardening due to the carbide forming properties of molybdenum [31].*

2.6. Effect of alloying elements

The alloying elements in steels affect both the thermodynamic and kinetic properties of the steels. Due to the numerous alloying elements available, this section will focus on the main elements in F22 steel: carbon, chromium, manganese, molybdenum, nickel and silicon.

Carbon is the main alloying element in steel, and is present for its strengthening effect. Manganese and silicon are common elements in modern steelmaking, and can in most steels be considered remnants of the production process. Nickel will generally enhance the properties of the steel, especially at low temperatures by increasing its toughness, as well as by stabilizing the oxide layer at the steel surface, making the steel less susceptible to corrosion. Molybdenum is also known for its ability to stabilize oxide layers.

The addition of chromium and molybdenum delays the ferrite-pearlite reaction, increasing the hardenability of the steel. Almost all alloying elements will delay the ferrite-pearlite reaction, but chromium and molybdenum are present in much larger amounts than the other alloying elements in F22 steel. The effect of molybdenum is shown in Figure 8, where addition of molybdenum has separated the ferrite-pearlite and bainite reactions in the TTT-diagram.

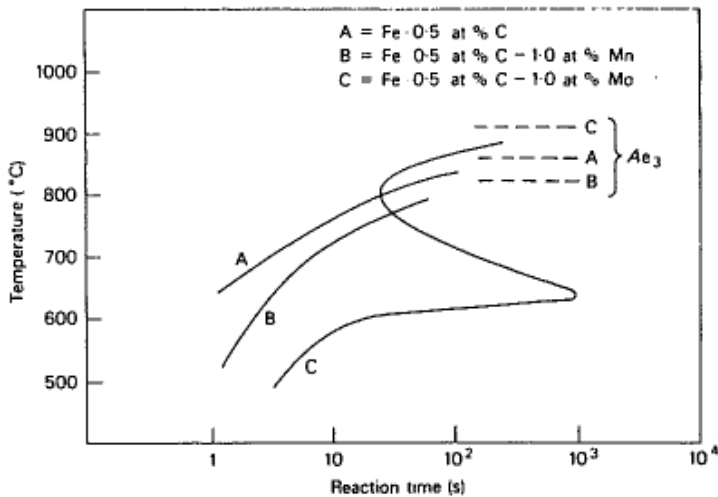


Figure 8: *Effect of different alloying elements on the TTT-diagram of a Fe-0.5 at% C steel. The effect of molybdenum in depressing the γ/α -reaction can be seen as the “bay” between the bainite and ferrite fields in curve C. The dashed lines show the ferrite stabilizing properties of molybdenum, since increased molybdenum content increases the Ae_3 [32].*

Most alloying elements, with the exception of cobalt and aluminium will lower the M_s temperature. The effects of other alloying elements are shown in Equation 3, which is an empirical relation by Andrews linking M_s and alloy contents (concentrations in wt%) [20, pp. 116–117].

$$M_s[^\circ C] = 539 - 423(\%C) - 30.4(\%Mn) - 17.7(\%Ni) - 12.1(\%Cr) - 7.5(\%Mo) \quad (3)$$

2.7. Production and processing of F22 steel

The steel investigated in this master’s work, F22, is a quench-temper (QT) steel, where the “F” indicates a forged steel. The properties of this steel comes from being forged, followed by quenching and tempering. Forging results in a fine grained microstructure, which is capable of both high strength and high toughness.

After the final forging is finished, the steel is austenitized and quenched in water. This produces a martensitic microstructure, which is then tempered at high temperatures ($\sim 650^{\circ}\text{C}$) for a long time (>3 hours) to produce a tough microstructure. Tempered martensite is a microstructure known to have one of the best combinations of strength and toughness available.

The microstructure of F22 steel should consist of heavily tempered martensite laths, where cementite or carbides of molybdenum or chromium have been precipitated and spheroidized. If the tempering process has taken place at temperatures close to 700°C , recrystallization of martensite laths can have taken place.

2.8. Forge welding

FMC Technologies is assessing the SAG-FW-process (Shielded Active Gas Forge Welding) for the production of riser pipes. The basic principle of forge welding is to austenitize the surfaces to be joined before forcing the two surfaces together with an impulsive force. A typical joining temperature is $1100\text{--}1200^{\circ}\text{C}$, and typical joining pressure is 1.5 tons per cm^2 of nominal surface. This procedure causes the material to yield and flow plastically, which creates a metallic bond between the surfaces [33]. The general concept of forge welding with active gas is shown in Figure 9.

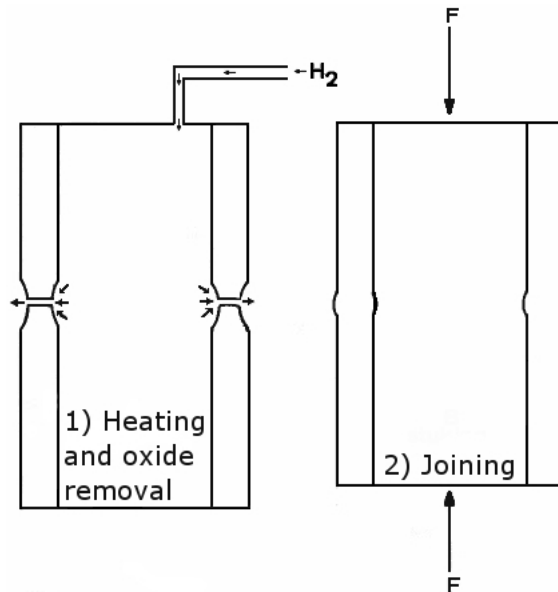


Figure 9: *Schematic sketch of the general forge welding process. Modified from Moe [33].*

The SAG-FW-process utilizes high-frequency resistive heating (HFR-heating) by attaching electrodes to the mating joints and running an AC-current through the

joint area. In addition, a gas cover is attached to flush the surfaces with a reducing gas to remove oxide layers before joining, as well as to prevent formation of oxide layers during heating and joining.

The SAG-FW-process has proven to be able to produce high quality joints faster than traditional fusion welding [33]. The main disadvantage of the process is its comprehensive set-up, making large production quantities a necessity for implementation to be economical.

2.9. Previous work on strength-hardness relations

Establishing relations between strength and hardness is not a new idea. Already in 1951, Tabor [14] found the relation given by Equation 4,

$$R_m = \left(\frac{HV}{2.9} \right) (1 - n) \left(\frac{12.5n}{1 - n} \right)^n \quad (4)$$

which relates the ultimate, nominal stress, R_m , to the Vickers hardness, HV , and the strain hardening coefficient, n . Note that the traditional unit for hardness is kg_f/mm^2 , while stress is usually given in N/mm^2 . This leads to a unit difference of $9.81 \text{ N}/\text{kg}_f$. Tabor assumed the true stress, σ , could be approximated by the following equation:

$$\sigma = K \varepsilon^n \quad (5)$$

where K is a constant and ε is the true strain. This equation makes it possible to determine n from experimental results. A simplified derivation results in the following expression when the curve is only fitted for the (A_{gt}, R_m) -point of the tensile curve:

$$n = \ln(1 + A_g) \quad (6)$$

The strain hardening coefficient can also be calculated by determining the slope of $\ln \sigma$ plotted against $\ln \varepsilon$. If the tensile curves will not produce a straight line with Equation 5, the Ludwik equation, $\sigma = \sigma_0 + K \varepsilon^n$ can be used to obtain a straight line [34, p. 288].

The relation shown in Equation 4 was improved by J.R. Cahoon [16], who in 1972 presented the relation shown by Equation 7.

$$R_m = \frac{HV}{2.9} \left(\frac{n}{0.217} \right)^n \quad (7)$$

Cahoon claimed this relation to be both simpler and more accurate when compared to the relation found by Tabor. Even Tabor noted that his relation showed good

correlation for lower values of the strain hardening coefficient, n , but not for higher values of n . Cahoon claims that his relation provided a good fit for all values of n [16].

There have been fewer attempts at establishing relations between the 0.2 % offset yield strength and the hardness of metals. According to Cahoon et al. [15], their relation was the first attempt at establishing a relation between yield strength and hardness. The result is shown by Equation 8.

$$R_{p0.2} = \frac{HV}{3} 0.1^n \quad (8)$$

The relations presented by Equations 4, 7 and 8 are good estimates for various alloys, but are all dependent on prior knowledge of the specific material, since the strain hardening coefficient is a part of the expression.

In order to provide relations between strength and hardness, depending solely on bulk material hardness, Pavlina and Van Tyne [13] set out to correlate 20 years of test results. Their work resulted in the expressions shown by Equations 9 and 10.

$$R_{p0.2} = 2.876 \cdot HV - 90.7 \quad (9)$$

$$R_m = 3.734 \cdot HV - 99.8 \quad (10)$$

Note that the input for these equations is the Vickers hardness with unit kg_f/mm^2 , and that their output is the strength value in MPa or N/mm^2 . These equations are linear approximations based on measurements of strength and hardness of more than 150 non-austenitic, hypoeutectoid steels with varying composition and microstructure. They also provided correlations sorted by microstructure in order to increase the precision of the regressions.

Pavlina and Van Tyne found that their correlations gave fairly large standard errors, and believed this to be caused by having left out the strain hardening coefficient in the expression for the strength. In order to overcome this, they invented an average strength, which would be the average between the yield and tensile strength for a specific steel. This gave more stable results and reduced the standard deviation [13].

3. Experimental

The following section will describe the experimental equipment and procedures. The investigations can be divided in two: The first investigations were performed to complement the findings of the present author during investigations of F22 steel [12], and consisted of tensile testing of the base material and weld simulation and tempering with accompanying hardness measurements and tensile testing. The second part consisted of establishing a relation between strength and hardness for F22 steel. All investigations were performed with the same F22 steel.

3.1. Material

The investigations started with a study of the same F22 material as investigated by the present author [12], in order to supplement the findings from the previous project. The composition of this material is shown in Table 1.

The steel had been produced by former Acciaierie Grigoli, now Verona Steel, and had been forged by La Forgia Di Bollate. The material came from a “box end connector dual bore” testpiece. It was in the shape of a steel pipe, 250 mm long, with 232 mm outer diameter, and 29 mm wall thickness.

Table 1: *Chemical composition of F22 steel. Same steel as investigated in [12].*

Element	wt%
C	0.120
Mn	0.350
Si	0.130
P	0.006
S	0.004
Cr	2.200
Ni	0.120
Mo	0.930
Cu	0.100
V	0.003
Al	0.034
Nb	0.002

The test material had been austenitized at 980°C for 7 hours, quenched in water and tempered at 640°C for 14 hours before being air cooled to ambient temperature, as shown by the material certificate (Appendix A.4, p. 77). The material certificate following the steel provided information of the material’s mechanical properties. These are shown in Table 2.

Table 2: *Mechanical properties of received F22 steel, according to the material certificate. As shown in Appendix A.4 (p. 77).*

Feature	Value
Yield strength	616 MPa
Tensile strength	738 MPa
Elongation	24 %
Area reduction	73.8 %
Average impact toughness at -40°C	163 J
Brinell hardness	235 HB \approx 247 HV

3.2. Heat treatment

3.2.1. Weld simulation

Specimens for weld simulation, measuring 11x11x100 mm, were machined by the faculty workshop, see Figure 10 for illustration.

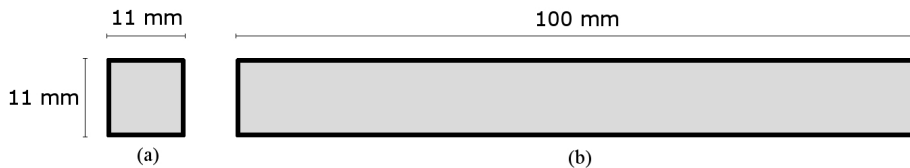


Figure 10: *Dimensions of weld simulated samples.*

- a) *Cross section.*
- b) *Longitudinal section.*

Weld simulations were performed using a “SMITWELD Thermal Cycle Simulator model 1405”, from this point on referred to as Smitweld. It is a system for thermal simulation of welding. Smitweld has a user interface consisting of two water cooled jaws, see Figure 11, and works by conducting a current through the sample linking the two jaws. This provides resistive heating of the sample. A thermocouple is spot welded to the specimen surface, and makes it possible for Smitweld to run according to the programmed temperature. Heating rate, cooling rate and holding time are determined and programmed by the user. Smitweld was operated in the linear mode, which means that straight lines connect each programmed time and temperature, as shown by Figure 12.

Figure 12 show the cycles programmed in Smitweld. The heating rate was set to 140°C/s for all samples. Peak temperature was set to 1160°C in order to compensate for deviations in Smitweld’s temperature control, which resulted in measured peak temperatures of approximately 1144°C. The aim was 1150°C, which is a typical joining temperature for forge welding.

The weld simulated samples were cooled at two different cooling rates: 10 and

60°C/s. These cooling rates are similar to those obtained on respectively the inner and the outer surfaces of forge welded pipes, and will therefore represent respectively root and cap regions of the weld cross section when compared to the requirements for welds in riser pipe material.

A total of 14 specimens were weld simulated according to the cycles shown in Table 3.

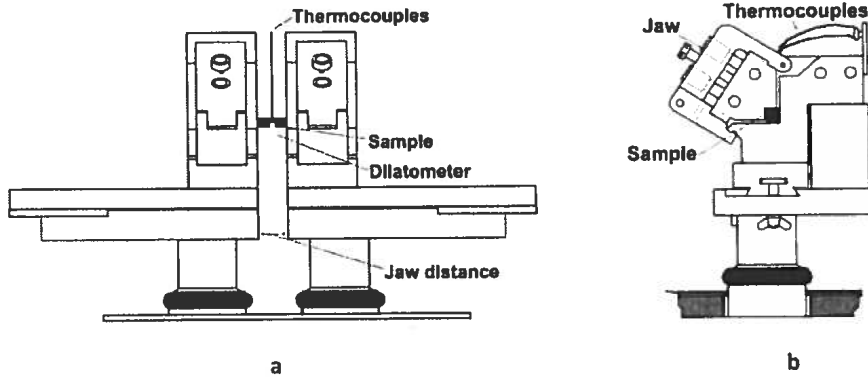


Figure 11: User interface of Smitweld. Modified from Samardžić and Dunder [35].

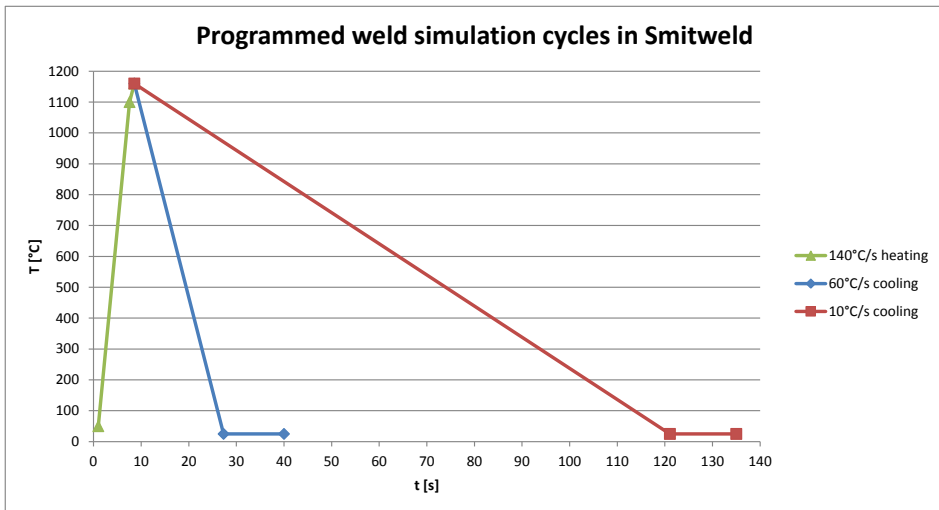


Figure 12: Graphic presentation of the weld simulation cycles programmed for Smitweld. The coordinates of the data points represent the values programmed into Smitweld. An example of this is ($t= 8.56$ s, $T= 1160^{\circ}\text{C}$), which is the peak of the curve.

Table 3: *Simulation schedule for weld simulation. Tempering was performed in furnace (Section 3.2.2).*

T_{peak}	C.R. [°C/s]	T_{temper} [°C]	t_[temper] [hours]	Parallels
1150	10	-	-	1
1150	60	-	-	1
1150	10	650	1/3/6	2/2/2
1150	60	650	1/3/6	2/2/2

3.2.2. Tempering

Tempering was performed in a “Nabertherm N 11/R” furnace with a C 19 control panel and a “Nabertherm N 17/HR” furnace with a C290 control panel at respectively 600°C and 650°C. The furnaces were preheated to the tempering temperature before the specimens were placed in the furnace chambers. The temperature was monitored by both integrated furnace thermocouple and an external K-type thermocouple placed in the centre of the furnace chamber. Samples were, when possible, placed standing in the furnace, and were allowed to air cool to ambient temperature after tempering. The tempering schedules are shown in the sections linked to the particular investigation.

3.2.3. QT-heat treatment

Hardening and tempering of F22 steel was performed to provide variations in strength and hardness, thereby making it possible to establish a strength-hardness relation valid for a wide range of heat treatments.

Prior to heat treatment, investigations regarding decarburization were carried out. These involved placing 3 specimens measuring 10x10x25 mm in a “Nabertherm N 17/HR” furnace preheated to 1200°C. Sample 1 had a hole drilled into its centre, and a K-type thermocouple inserted to determine the time necessary before the core of the sample reached furnace temperature. Temperature was logged using a “Fluke 54 II Thermometer”, from now on referred to as Fluke. Sample 2 was kept in the furnace for 10 minutes before it was quenched in water. Sample 3 was kept in the furnace for 30 minutes before being quenched in water. Sample 2 and 3 were cut at mid length using a “Struers Discotom 5”. This produced two 12 mm long pieces where the cross sections were embedded, ground and polished. Microhardness was measured using a “Leica WMHT MOT”. The measured values were compared with theoretically calculated values for decarburization, and good compliance between measured and calculated values were obtained. These investigations revealed the amount of material which had to be removed after heat treatment, due to decarburization. The results are shown in Appendices A.9 and A.8 (pp. 82–81).

Further preliminary investigations regarding heating rate were carried out on a

specimen with the same cross section as those being machined into tensile specimens. A K-type thermocouple was drilled into the centre of the sample, and the sample was placed in a preheated furnace at 600° and 650°C. Two other samples, one large and one small, were placed in a furnace preheated to 1200°C. The heating and cooling rates were logged using a Fluke, and used to determine the necessary time in the furnace for hardening. The heating and cooling rates from heating to 600°C and 650°C were used to calculate the tempering effect for samples not having reached furnace temperature. The results are shown in Appendix A.8 (p. 81). The F22 steel proved to have high hardenability, since even air cooling produced martensitic microstructures.

Heat treatment started with obtaining samples of roughly cut F22 steel, without exact dimensions, but with the requirement for the piece to be large enough to machine two tensile specimens from the material after heat treatment. The steel was austenitized in a Nabertherm N 17/HR furnace, quenched in water and tempered in the same furnace or a Nabertherm N 11/R furnace. The steps in the heat treatment are shown below:

1. Austenitizing at 1200°C for 20 minutes.
2. Quenching in water.
3. Tempering at 600°C or 650°C. Samples were left to air cool to ambient temperature after tempering.

The QT-treatment was originally intended only for specimens to be machined into tensile specimens. In addition to these samples, several samples for microstructural investigation were heat treated to document the microstructures obtained.

In order to verify the accuracy of the Hollomon-Jaffe tempering relationship (Equation 2, p. 10), two tempering series were conducted. All samples were hardened at 1200°C, while tempering was performed at two different temperatures. The tempering time was calculated, according to the Hollomon-Jaffe parameter, to produce the same tempering effect/hardness reduction. Since these specimens were machined into tensile specimens and their hardness was measured, see Sections 3.4 and 3.3.2, it was possible to investigate if an equal reduction in hardness was obtained by utilizing the Hollomon-Jaffe relationship, as well as seeing if an equal reduction of hardness directly equalled reduction of strength.

Tempering was performed at 600°C and 650°C. The tempering schedule is shown in Table 4.

When establishing a relation between strength and hardness it is often considered of interest to have a relation valid for a wide range of strength and hardness. In order to achieve this, three samples with accompanying microstructure samples went through controlled cooling after having been austenitized at 1200°C. Their three different cooling cycles were:

1. Sample left in furnace and allowed to cool slowly to room temperature during the following 24 hours. The cooling time between 800°C and 500°C, $\Delta t_{8/5}$, was 4 hours. Corresponding cooling rate was 0.02°C/s.
2. Sample placed in furnace at 700°C for 6 hours, removed from furnace and air cooled to ambient temperature.
3. Sample placed in salt bath at 600°C for 30 hours, removed from salt bath and air cooled to ambient temperature.

The temperatures and holding times were chosen according to the IT-diagram shown in Figure 4 (p. 7), with the goal of obtaining ferrite-pearlite structures with varying grain size and varying pearlite lamellae spacing.

Table 4: *Tempering performed after hardening of QT-samples. Time was measured from the samples were placed in the furnace until they were removed, without taking heating time into consideration. The three ferrite-pearlite samples and their heat treatments are not shown in this table.*

#	T_{temper}	t_{temper}
1	-	-
1	600	7 minutes
1	600	13 minutes
1	600	41 minutes
1	600	15 hours and 8 minutes
1	600	48 hours and 20 minutes
1	650	5 minutes
1	650	10 minutes
1	650	30 minutes
1	650	1 hour
1	650	3 hours

3.3. Vickers hardness measurements

3.3.1. Weld hardness profiles

Vickers hardness was measured using a “Struers Duramin A2500” with 10 kg loading force, 100 $\mu\text{m/s}$ loading speed and 15 s loading time. Prior to the hardness measurement, the samples were ground to remove 0.5 mm of material. This was done in order to remove decarburized surface material before the hardness measurement. The samples were then prepared with grinding, polishing and etching in order to reveal the heat affected zone, see Section 3.6 (p. 26) for detailed description of surface preparation.

In order to ensure the reliability of the hardness measurements, a series of micro-hardness measurements were performed. This test was done to investigate whether

large fluctuations in hardness were observed along the depth profile due to decarburization from weld simulation and tempering. The resulting hardness profile is shown in Appendix A.7 (p. 80). No noticeable hardness variations were observed.

Hardness was measured as 17 indentations across the heat affected zone. A line of 15 indentations, each separated by 1 mm, spanned from unaffected base material, across the heat affected zone and into the other side of unaffected base material. In addition, 2 extra indentations were placed in the “weld centreline”. Figure 13 illustrates the placement of the indentations.

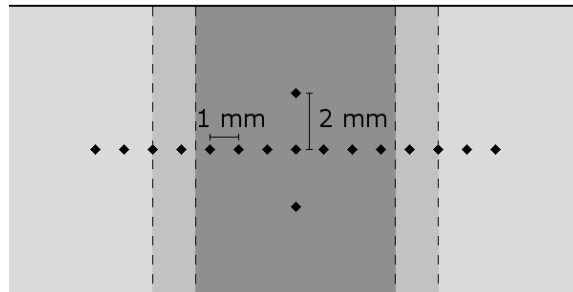


Figure 13: *Sketch showing the indentation pattern along a weld simulated sample. Darker areas indicate more severely heat affected zones.*

3.3.2. Hardness of tensile specimens

The hardness of tensile specimens was measured using a “Struers Duramin A2500” and a “Matsuzawa DVK-1S” with 10 kg loading force, 100 $\mu\text{m/s}$ loading speed and 15 s loading time. Hardness of the quenched and tempered specimens, as well as the ferrite-pearlite specimens, was measured using the Matsuzawa, while the Struers was used to measure the base material and weld simulated specimens. Two different machines had to be used due to technical problems with the Struers machine. Hardness was calculated as an averaged value based on 12 measurements on each tensile specimen. The 12 indentations were distributed as 3 indentations on each side of the specimen, as shown in Figure 14. Hardness was measured in the grip surfaces in order to avoid measurements in work hardened material.

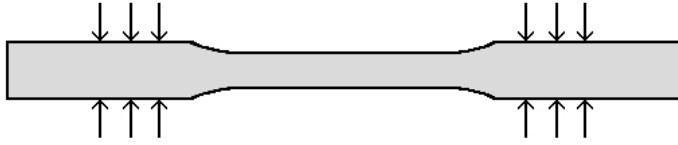


Figure 14: Placement of hardness indentations on tensile specimens.

3.4. Tensile testing

Tensile testing was carried out on material having been subjected to several different heat treatments, in addition to testing of base material. The heat treatments for the weld simulated samples are shown in Table 5. Quenched and tempered samples were also machined into tensile specimens. Their heat treatments are shown in Table 4 (p. 22). From each quenched and tempered sample, two tensile specimens were machined.

Yield strength was determined as offset yield stress. This was determined as the stress producing a permanent deformation of $A = 0.002$. In other words: The stress found by adding a strain of 0.002 to the strain at the end of the linear section of the stress-strain curve.

Table 5: Heat treatment schedule for weld simulated and base material tensile specimens. First row presents samples not subjected to heat treatment in order to test base material. Second and third row are weld simulated, untempered samples for comparison of strength with that of base material.

T_{peak} [°C]	C.R. [°C/s]	T_{temper} [°C]	$t_{[\text{temper}]}$ [hours]	Parallels
-	-	-	-	3
1150	10	-	-	2
1150	60	-	-	2
1150	10	650	1/3/6	3/3/3
1150	60	650	1/3/6	3/3/3

The specimens for tensile testing were machined by the faculty workshop. Two different dimensions were used for the tensile specimens. The 25 first samples (base material and weld simulated specimens) were machined according to the measurements shown in Figure 15. The 22 quenched and tempered specimens, as well as the 6 ferrite-pearlite specimens, had a shorter tapered region, as shown in Figure 16.

During testing of the first 25 specimens having the old dimension, fracture occurred close to the knife of the extensometer in 14 of the specimens. These specimens had a significantly lower recorded elongation than the other specimens, in which fracture took place closer to the centre of the tapered region. In order to reduce the possibility of unrecorded elongation taking place outside the 25 mm extensometer,

the parallel, tapered region was shortened from 30 to 26 mm for the remaining samples, as shown in Figure 16. The result was fractures close to the extensometer in 5 out of 28 samples, where only 3 of the fractures were close enough to affect the recorded elongation significantly. Still, the improved results could also originate from the absence of a HAZ, leaving more of the parallel region as potential point of fracture.

Tensile testing was performed using a “MTS 810” hydraulic tensile machine. A 25 mm extensometer recorded elongation.

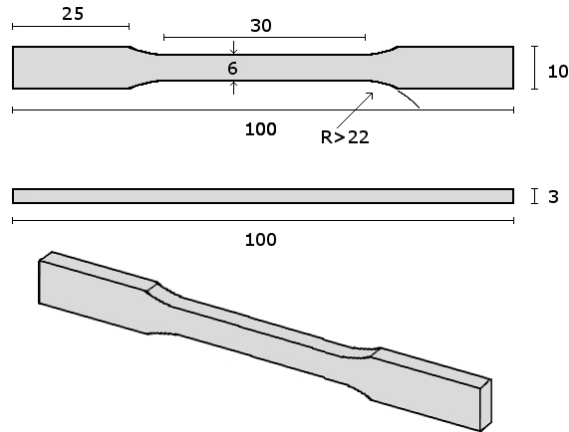


Figure 15: *Dimensions of the 25 first tensile specimens used for testing of weld simulated and base material .*

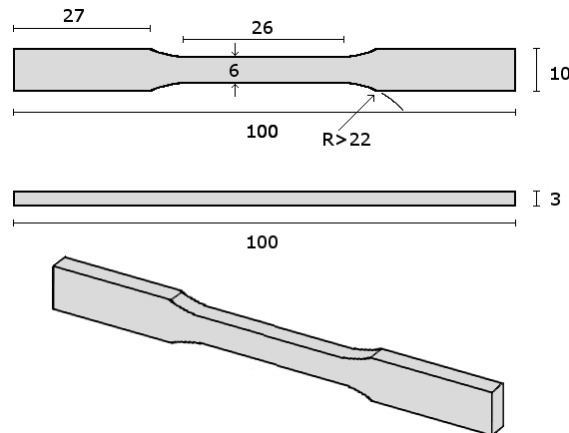


Figure 16: *Dimensions of modified tensile specimens. Length of tapered region reduced from 30 to 26 mm by increasing grip areas. Used for testing of quenched and tempered material as well as samples subjected to controlled cooling or isothermal heat treatment.*

3.5. Data analysis and statistics

The establishment of a relation between strength and hardness has led to a certain amount of data analysis: 732 hardness indentations and 61 yield and tensile strengths have been produced.

The hardness values in the strength-hardness relation were calculated as an averaged value from 12 indentations on each tensile specimen. From these results, the standard deviations were calculated using the following formula [36, p. 15]:

$$\sigma_{HV} = \sqrt{\frac{\sum_{i=1}^n (HV_i - \overline{HV})^2}{n-1}} \quad (11)$$

The standard deviation was then normalized with respect to the mean hardness number and expressed as a percentage value using the following formula to make it a directly comparable number regardless of mean sample hardness:

$$\sigma_N = \frac{\sigma_{HV}}{HV} \cdot 100\% \quad (12)$$

The following equation was used for calculating the standard deviation for the regressions correlating strength and hardness [36, p. 402]:

$$\sigma = \sqrt{\frac{\sum_{i=1}^n (R_i - \hat{R}_i)^2}{n-2}} \quad (13)$$

3.6. Metallographic preparation

As described in a previous section, 7 microstructure samples were austenitized and quenched or cooled with varying cooling rates in order to examine the obtained microstructure. The various heat treatments of the microstructure samples are as follows:

- Cooled in furnace from 1200°C to ambient temperature.
- Removed from furnace at 1200°C and placed in furnace at 700°C for 6 hours. Air cooled to ambient temperature.
- Removed from furnace at 1200°C and placed in salt bath at 600°C for 30 hours. Air cooled to ambient temperature.
- Quenched from 1200°C in water and tempered for 7 minutes at 600°C.
- Quenched from 1200°C in water and tempered for 48 hours at 600°C.
- Quenched from 1200°C in water and tempered for 5 minutes at 650°C.

- Quenched from 1200°C in water and tempered for 3 hours at 650°C.

The samples were cut in the transverse direction, approximately 15 mm from the end, and embedded in Epofix. Grinding and polishing were performed with a fixed sample holder, utilizing the Struers RotoPol- and TegraForce-systems. For this; 120, 320, 500, 1200, 2400, 3 µm and 1 µm grit was applied. For etching, 2 % Nital solution was used. Quenched samples with martensitic structure were etched for 45 seconds, while samples with ferrite-pearlite structure were etched for 20 seconds.

Obtaining an even etch on the sample surface proved to be difficult, especially for quenched and tempered samples. This is believed to be caused by the high contents of chromium in F22 steel. A general rule of thumb states that chromium equivalent to five times the amount of carbon can be precipitated as chromium carbides. According to the rule of thumb, with a carbon content of 0.12 wt% and a chromium content of 2.20 wt%, this leaves 1.6 wt% chromium dissolved after tempering. This chromium can form an oxide layer resisting the corrosion of the etchant, especially when backed up by the oxide stabilizing elements molybdenum and nickel which are also present in F22 steel. In addition to this, molybdenum can precipitate as carbides, leaving more dissolved chromium for forming a stable oxide layer. Due to this, the etching time for martensitic samples had to be increased from 20 to 45 seconds.

3.7. Microscopy and microhardness

A “Leica MEF4M” light microscope was used for metallographic examination and imaging of the specimens. Images were recorded with 20x and 100x objective lenses, using “Image Access EasyLab” software and “Jenoptik ProgRes C10 plus” camera.

A “Leica VMHT MOT” was used for microhardness measurements. This was done to provide further information concerning the microstructures observed in the light microscope. The load was varied between 25 and 100 g in order to fit the indentation to the size of the constituent.

3.8. SEM investigation

A “Zeiss Ultra 55, Limited Edition FESEM” was used for imaging and EDS analysis. Etched samples from the metallographic investigation were attached to a specimen holder with carbon tape and placed inside the vacuum chamber. They were imaged with secondary electron detector at 40 000x magnification with 120 µm aperture, 15 kV acceleration voltage and high current mode activated. The working distances were kept between 9 and 12 mm. In addition, EDS analysis of carbide precipitates was performed. For this, a Bruker detector and Esprit software was used.

In order to ensure that there were no differences in the imaged structures, some of the samples were marked with hardness indentations and imaged with both SEM

and light microscope to ensure that the imaged structures were comparable. These results are shown in Figure 24 (p. 42).

EDS analysis will excite electrons from a certain volume of the sample, and for iron, the emission depth at 15 kV acceleration voltage is approximately 0.9 μm [37, p. 100]. The carbides present in the investigated samples were much smaller than 0.9 μm . In order to reduce emission from the surrounding matrix, the acceleration voltage was reduced from 15 kV to 8 kV. This reduced the emission depth from approximately 0.9 μm to 0.3 μm .

4. Results

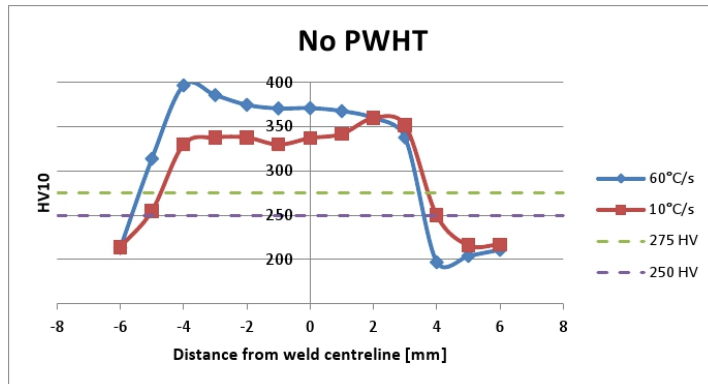
The results section can be divided in two parts: 1) Investigations regarding forge welding. 2) The establishment of a relationship between strength and hardness for F22 steel.

4.1. Forge welding investigations

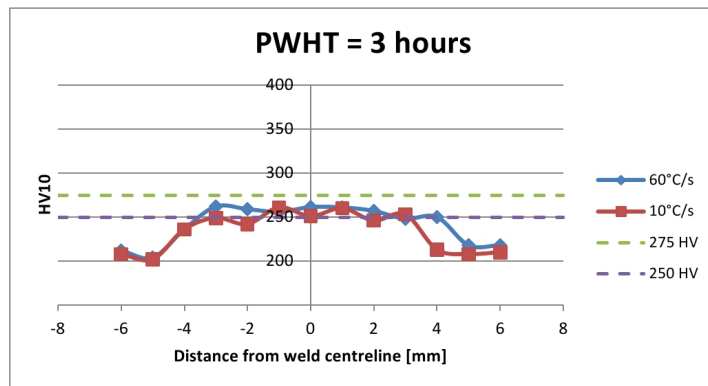
4.1.1. Hardness profiles

Hardness measurements across the HAZ of material subjected to thermal forge welding simulations provided the data necessary to plot weld hardness profiles. Figure 17 shows results previously obtained by the present author [12], while Figure 18 shows new hardness profiles obtained during this master's work.

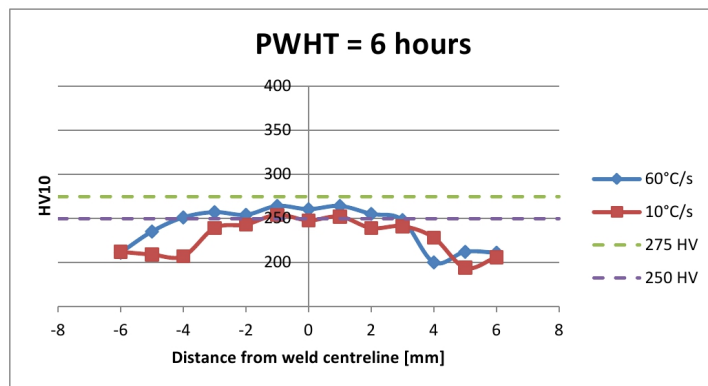
The graphs show that tempering at 650°C is more effective than tempering at 625°C. Higher tempering temperature resulted in faster hardness reduction, as well as reducing the hardness more than tempering at 625°C. Comparing the graphs in Figures 17c) and 18b) reveal a higher reduction in hardness from tempering for 3 hours at 650°C than from tempering for twice as long, 6 hours, at 625°C.



(a)

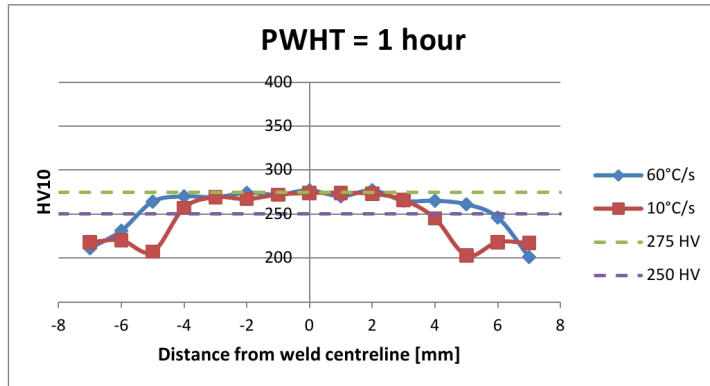


(b)

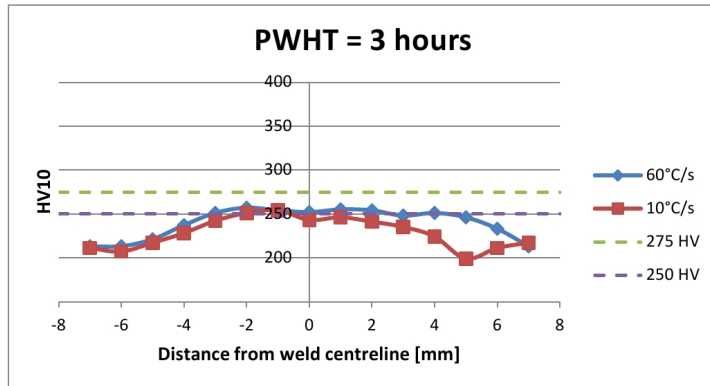


(c)

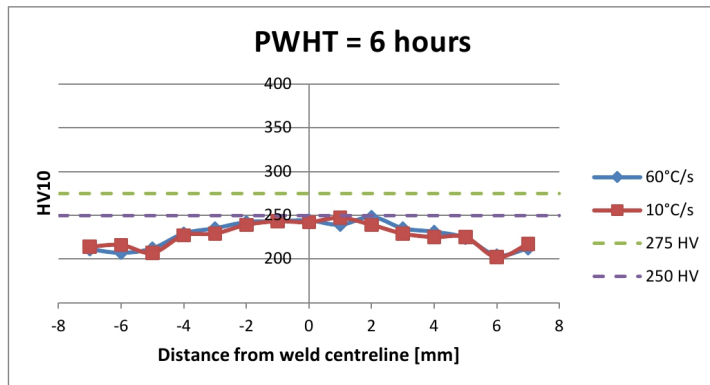
Figure 17: Weld hardness profiles from previous investigations by the present author [12]:
 a) Profile from sample not subjected to PWHT.
 b) Profile from sample tempered for 3 hours at 625° C.
 c) Profile from sample tempered for 6 hours at 625° C.



(a)



(b)



(c)

Figure 18: Weld hardness profiles from the present investigations:
 a) Profile from sample tempered for 1 hour at 650° C.
 b) Profile from sample tempered for 3 hours at 650° C.
 c) Profile from sample tempered for 6 hours at 650° C.

4.1.2. Hardness development during tempering

The hardness development during tempering was found from samples used for weld hardness profiles. For each tempering time and cooling rate, 3 indentations were made along the weld centreline, and the average hardness value was calculated. Largest deviation from averaged value was 11 HV.

Figure 19 shows the hardness development during tempering. The curves reveal that 3 hours of tempering at 650°C was necessary to meet with requirements for hardness. Compared to the dotted curves obtained during tempering at 625°C in the previous work [12], the hardness seems to decrease faster during tempering at 650°C, but less experimental data makes a direct comparison difficult. In addition, a larger final hardness reduction was achieved after tempering for the same time at higher temperatures.

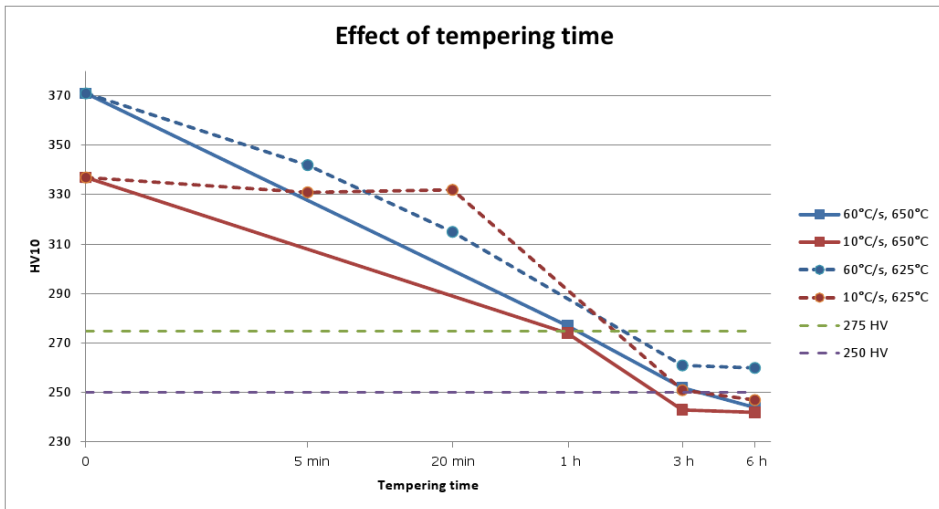


Figure 19: Hardness development as a function of tempering time. Requirements for hardness are shown as dashed, horizontal lines. Values for untempered hardness and the curves for hardness reduction from tempering at 625°C were found during the previous work [12]. Plotted values calculated as average of 3 indentations in weld centreline. Maximum deviation was 11 HV.

4.1.3. Tensile testing

Tensile testing was performed for testing the strength of material having been subjected to various heat treatments. All results regarding strength are calculated as nominal stress, and the abbreviations used in Tables 6 and 7 are according to NS-EN 10002-1, as shown in Appendix A.2 (p. 76).

Tensile tests of base material and weld simulated material revealed large differences

when it came to elongation. The main reason is that the hard, strong HAZ of weld simulated material will not deform, leading to less elongation of weld simulated specimens. Another source of variations when recording elongation, is the location of the fracture. If the sample fractured in close proximity to the knife of the extensometer, some of the necked region might be located outside the extensometer, leading to less recorded elongation. This happened for 14 of the 25 samples. As a consequence of this, the sample geometry was changed for later tensile tests.

Base material The base material was subjected to tensile testing in order to verify the material properties. In addition to testing the pure base material, a set of samples were weld simulated, but not tempered, in order to verify that weld simulation would not affect the strength of the adjacent base material.

The base material samples were machined longitudinal to the pipe, at random locations in the pipe wall. This simplified machining, and since the purpose was testing and comparing the material strength with its requirements, strength variations according to placement in the cross section was not of interest. (Same strength requirement across the entire cross section.)

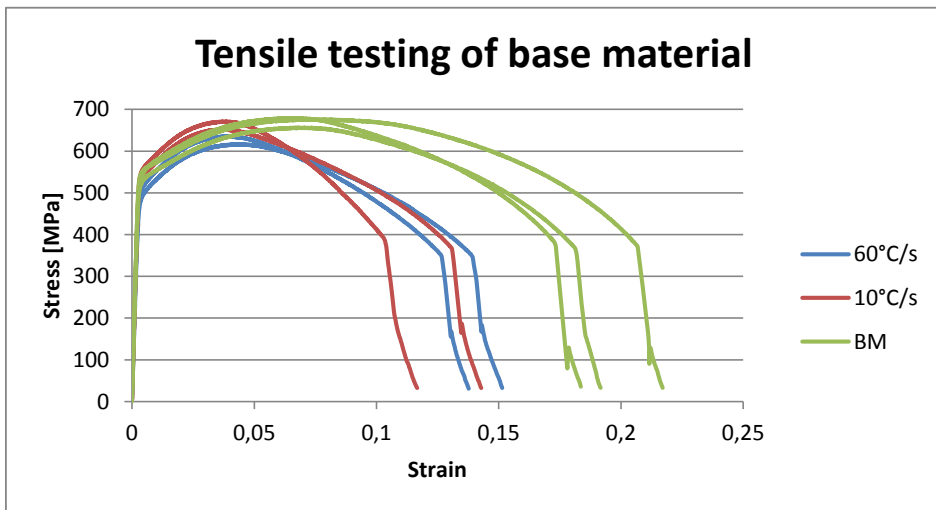


Figure 20: Tensile curves from testing of base material (BM) compared to curves from untempered, weld simulated material with cooling rates of 10° C/s and 60° C/s.

When comparing the averaged values shown in Table 6 with the requirements presented in the introduction and in Appendix A.1 (p. 75), it becomes evident that the base material suffers from insufficient strength. The requirements for yield to tensile ratio, elongation and area reduction are met, but both yield and tensile strength fail to satisfy the requirements. The complete results can be seen in Appendix A.3 (p. 76).

Table 6: *Averaged results from tensile testing of base material and untempered, weld simulated material (WS). The complete results can be seen in Appendix A.3 (p. 76).*

Condition	R_{p0.2} [MPa]	R_m [MPa]	R_{p0.2}/R_m	A^c [%]	Z [%]
Base material	548	671	0.82	19	68
WS, 10°C/s	550	662	0.83	12	68
WS, 60°C/s	506	626	0.81	14	69

The averaged values shown in Table 6, show that all strength values are within the same range, but that the specimens that were weld simulated and cooled at 60°C/s, were significantly weaker than the other samples. This is believed to be caused by defects in the weld simulation sample cooled at 60°C/s. Since both tensile specimens cooled at 60°C/s were machined from the same weld simulation sample, this is a plausible explanation.

Weld simulated and tempered material Tensile testing of weld simulated and tempered material was performed to see if the material could satisfy requirements to strength as given by FMC and shown in Appendix A.1 (p. 75). Averaged results (three parallels) can be seen in Table 7, while the complete results are shown in Appendix A.6 (p. 79). The accompanying stress-strain plots are shown in Appendix A.5 (p. 78).

Table 7: *Averaged results from each parallel of tensile tested, weld simulated and tempered material. All samples were tempered at 650° C. Cooling rate given in ° C/s.*

C.R.	t_t [h]	R_{p0.2} [MPa]	R_m [MPa]	R_{p0.2}/R_m	A^c [%]	Z [%]
10	1	561	678	0.83	16	66
60	1	560	673	0.83	13	66
10	3	547	669	0.82	17	68
60	3	547	663	0.83	16	68
10	6	537	656	0.82	18	67
60	6	539	656	0.82	14	67

It is evident from the results that tempering has an effect on the base material. Both yield and tensile strengths are clearly decreasing with increased tempering time.

None of the tensile specimens satisfied the requirements for yield and tensile strength given in the introduction and by Appendix A.1 (p. 75). The other requirements, except elongation, were satisfied by all samples. The poor elongation values were caused by the strong HAZ, as well as a short extensometer, as mentioned earlier in Section 4.1.3, not the material.

4.2. Strength-hardness relation

4.2.1. Metallographic investigation

A set of samples were heat treated to produce samples matching a selection of the microstructures having been subjected to tensile testing and hardness measurements. Light microscopy images from these microstructures are shown in Figures 21, 22 and 23.

The microstructures imaged in Figures 22 and 23 have ferrite-pearlite as their main constituent, while the microstructures imaged in Figure 21 contain mainly tempered martensite and some bainite. Figure 23 show the same microstructural elements as Figure 22, only with higher magnification.

The martensitic microstructures were tempered as two equi-tempered parallels with different temperature, but equal tempering effect. The Hollomon-Jaffe relation was used for a numerical calculation of the tempering effect, and the calculations were done based on measurements of core temperature from samples placed in the furnace at respectively 600 and 650°C (See Appendix A.8, p 81). Equal hardness is therefore expected in the samples tempered for 5 and 7 minutes, as well as for the samples tempered for 3 and 48 hours. This seems plausible with regards to microstructure where similar structures are observed in Figures 21a) and 21b) as well as in Figures 21c) and 21d).

The structure observed in Figures 22c) and 23c) was formed isothermally at 600°C during 30 hours. The microstructure contains grain boundary allotriomorph and Widmanstätten ferrite, as well as intragranular idiomorphs and plates. The main area fraction is a disordered main constituent. When referring to the IT-diagram for F22, Figure 4 (p. 7), it can be seen that 600°C is among the lower temperatures at which ferrite will form. It is therefore expected that the sample contains an increased fraction of pearlite. Since the sample has been kept at 600°C for such an extended period of time, it is believed that the formed pearlite has transformed into a form of spheroidized pearlite, which will from now on be referred to as degenerated pearlite. Additional SEM images of the microstructure are shown in Appendix A.13 (p. 86).

The same structure, degenerated pearlite, is observed in the sample cooled in the furnace to room temperature, see Figures 22a) and 23a). Since there is no doubt about the presence of pearlite in the furnace cooled sample, it is clear that the structure produced by isothermal treatment at 600°C must be degenerated pearlite. This is also confirmed by the microhardness measurements shown in Table 8, where the degenerated pearlite in both samples have similar hardness.

The same sample, shown in Figures 22c) and 23c) also contain other ferrite morphologies. In Figure 22c), Widmanstätten laths can be seen to the left in the picture, growing upwards from a prior austenite grain boundary covered by grain boundary allotriomorph ferrite. The structure also contains both intragranular idiomorphs and -plates, which can be seen in the upper left of Figure 22c).

Table 8 correlates the microstructures shown in Figure 22 to the averaged microhardness of the different phases.

Table 8: *Microhardness measurements of constituents present in ferrite-pearlite samples.*

Heat treatment	Hardness	Phase
Furnace cooled	133	Ferrite
	369	Degenerated pearlite
Treated isothermally at 700°C for 6 hours	165	Ferrite
	183	Coarse pearlite
	237	Fine pearlite
	625	Martensite
Treated isothermally at 600°C for 30 hours	287	Grain boundary allotriomorph ferrite
	317	Degenerated pearlite

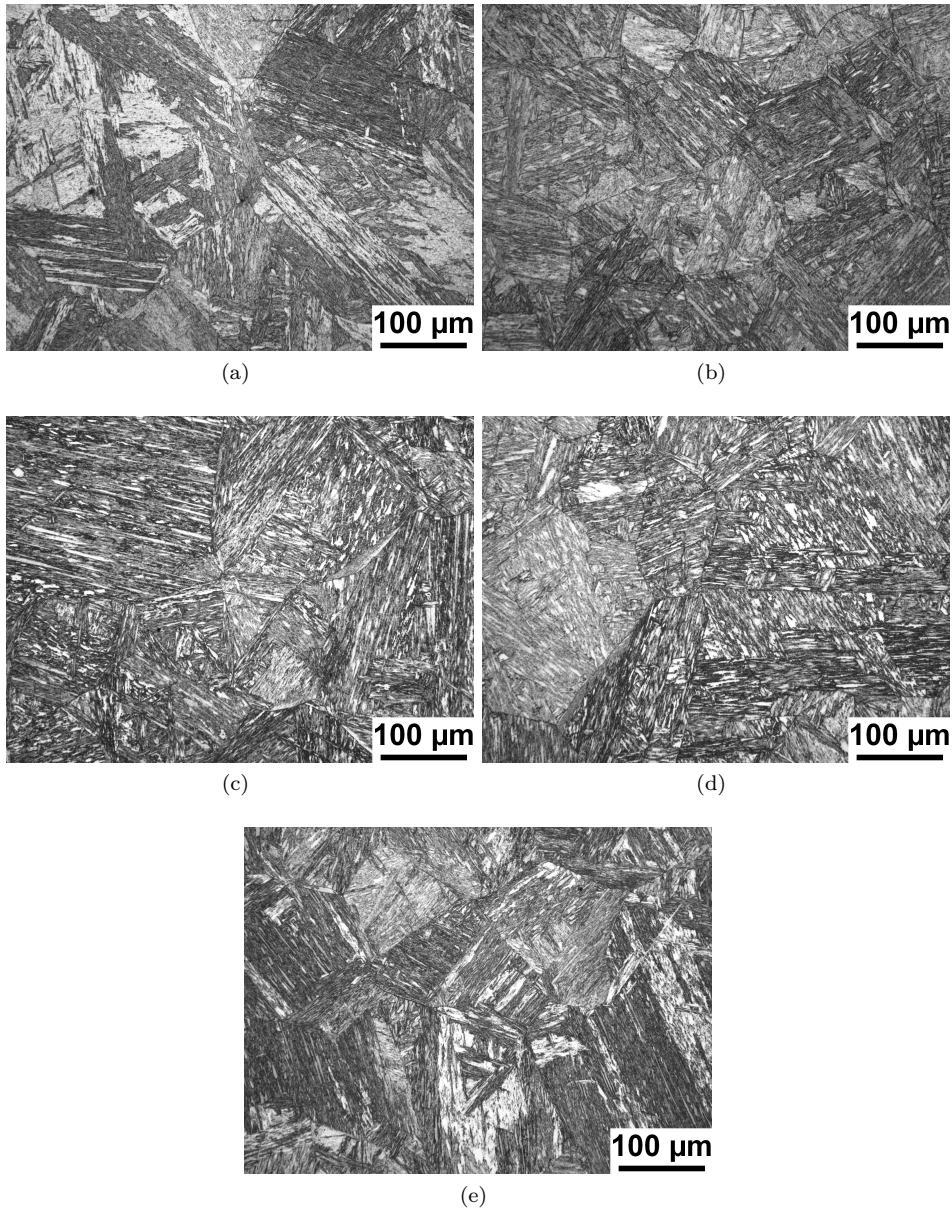
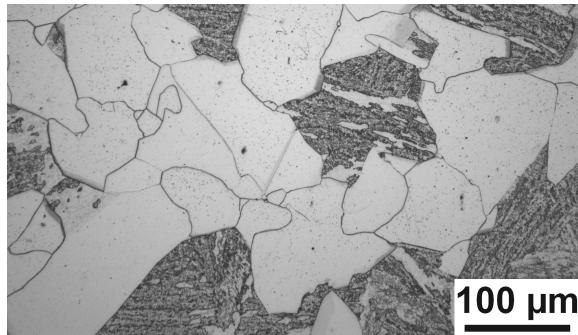
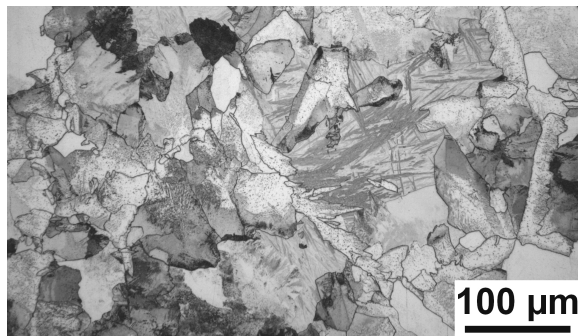


Figure 21: *Microstructure of quenched and tempered samples imaged with 20x objective:*

- a) Tempered at 600° C for 7 minutes.*
- b) Tempered at 650° C for 5 minutes.*
- c) Tempered at 600° C for 48 hours.*
- d) Tempered at 650° C for 3 hours.*
- e) As-quenched.*



(a)



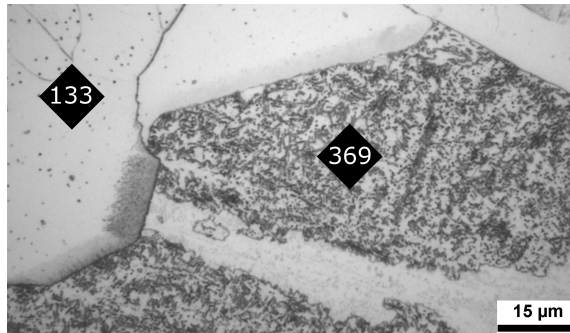
(b)



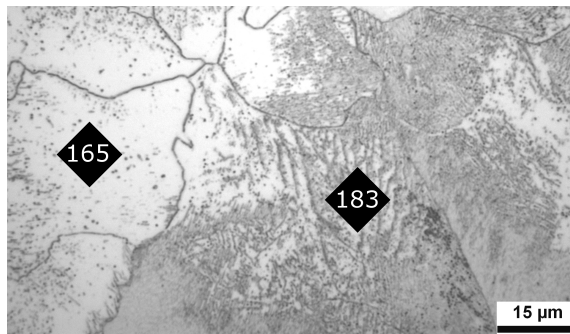
(c)

Figure 22: Microstructure of samples heat treated to obtain ferrite-pearlite structure imaged with 20x objective:

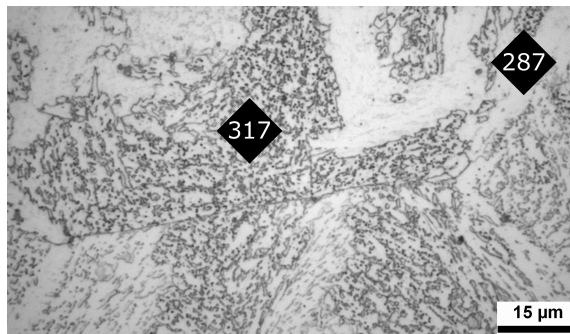
- a) Cooled in furnace to room temperature. Microstructure consists of ferrite and degenerated pearlite.
- b) Isothermally treated at 700°C for 6 hours. Microstructure consists of ferrite, martensite, fine and coarse pearlite.
- c) Isothermally treated at 600°C for 30 hours. Microstructure consists of degenerated pearlite, grain boundary allotriomorph ferrite, Widmanstätten ferrite, intragranular idiomorphs and intragranular plates. Upper and lower arrow indicate the location of respectively Widmanstätten- and grain boundary allotriomorph ferrite.



(a)



(b)



(c)

Figure 23: Same samples as shown in Figure 22 imaged with higher magnification (100x objective). Microhardness of the different phases are shown in the images:

- a) Cooled in furnace to room temperature. Microstructure consists of ferrite and degenerated pearlite.
- b) Isothermally treated at 700° C for 6 hours. Microstructure consists of ferrite, martensite, fine and coarse pearlite. The martensite and fine pearlite have not been imaged.
- c) Isothermally treated at 600° C for 30 hours. Microstructure consists of degenerated pearlite, grain boundary allotriomorph ferrite, Widmanstätten ferrite, intragranular idiomorphs and intragranular plates. The Widmanstätten ferrite and intragranular plates have not been imaged.

4.2.2. SEM-investigation

Two quenched and tempered samples were imaged and subjected to EDS analysis in SEM to document the development of carbides during tempering. The investigated samples were subjected to different heat treatments: Tempering for 7 minutes and 48 hours at 600°C, tempering for 5 minutes and 3 hours at 650°C, as well as an as-quenched sample. A sample treated isothermally for 30 hours at 600°C were also imaged with the SEM. These images are shown in Appendix A.13 (p. 86).

Figure 24 shows a comparison between the same microstructural element imaged with both SEM and light microscope. Hardness indentations were used as landmarks to ensure imaging of the same grain boundaries. This was done in order to ensure that the microstructural elements observed in the light microscope were correct when compared to the images from the SEM. The image from the light microscope has been cropped, inverted and digitally enlarged in order to accentuate that the two images show the same microstructural elements.

Images of the sample microstructures are shown in Figures 25, 26 and 27. These images reveal the changes of size and shape from prolonged tempering. The transition from lath-shaped to more spheroidized carbides can be clearly seen from Figures 25 and 26. The bottom arrow in Figure 25b) show two carbides which probably have spheroidized and split into two from one long, lath-shaped carbide. In addition, it can be seen that a larger area fraction of carbides is present in the samples subjected to prolonged tempering. The as-quenched sample shown in Figure 27 contains no visible carbides.

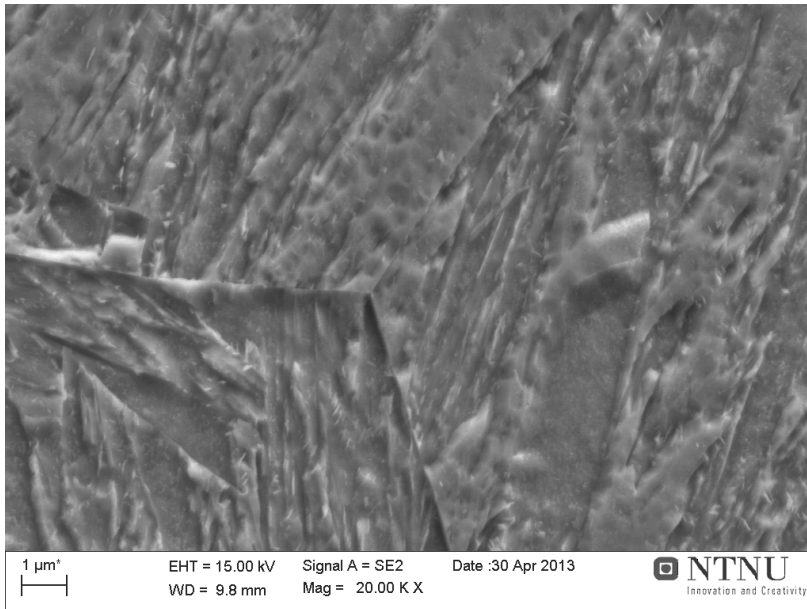
Images from EDS analysis (Figures 28 through 31) show that larger particles than the ones analysed were available for analysis, but the presented results are from smaller particles. The large particles were believed to be inclusions from the production process, which was supported by the EDS analysis, which revealed substantial amounts of oxygen in the largest particles.

The results from the EDS analysis are shown in Figures 28, 29, 30 and 31. Analysis of the carbide particles in the sample tempered for 7 minutes at 600°C showed that they had approximately the composition of the base material with regards to chromium and molybdenum content. The spectrum shown in Figure 28 shows that the carbon content is slightly higher in the carbide as compared to the carbon content in the matrix, which can be seen in Figure 29.

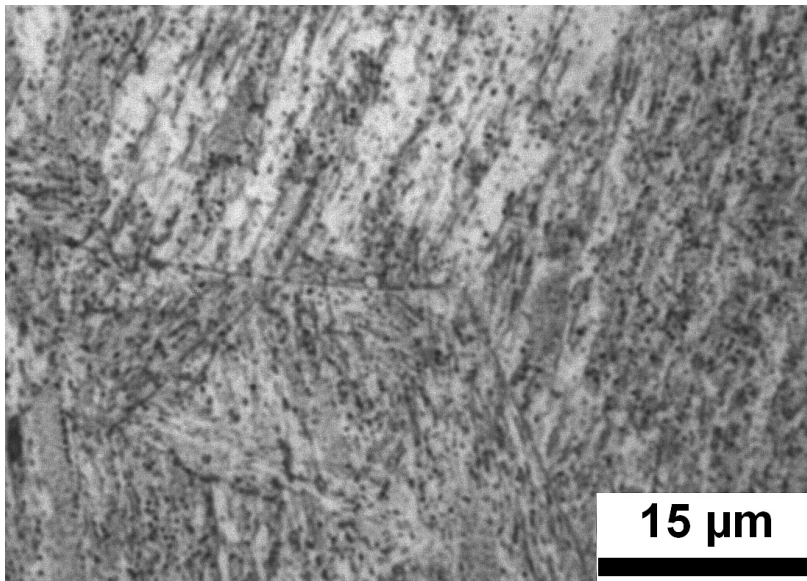
The carbides in the sample tempered for 48 hours at 600°C, on the other hand, contained higher amounts of chromium and molybdenum, as shown in Figure 30. Looking at the spectrum from the matrix, Figure 31, few peaks are present as compared to that from the particle. Still, a small amount of chromium, molybdenum and silicon can be observed as slight “bumps” in the background radiation. These are also present in both spectra from the sample tempered for 7 minutes (Figures 28 and 29).

When considering the EDS analysis, it is important to note that its results are

highly uncertain. They should be considered an indication, rather than as a quantitative result due to the amount of radiation from the matrix, and cannot be used for determining the composition of the carbides. There are several reasons why the results might be misleading: 1) The carbides were much smaller than the excitation volume, leading to production of X-ray signals from the surrounding base material as well as the carbides. 2) The samples were etched, leading to topographic effects. Despite their uncertainty, the results can still be used to confirm theory regarding carbide development, due to their qualitative differences.

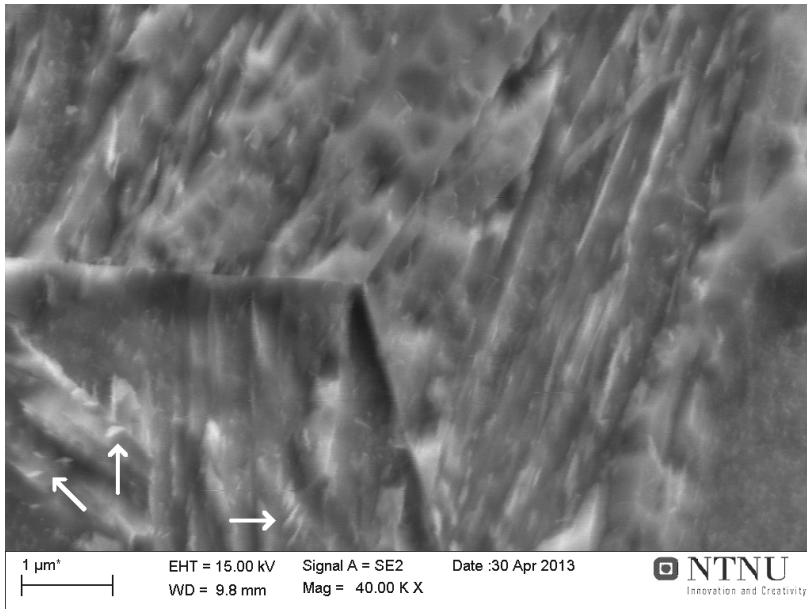


(a)

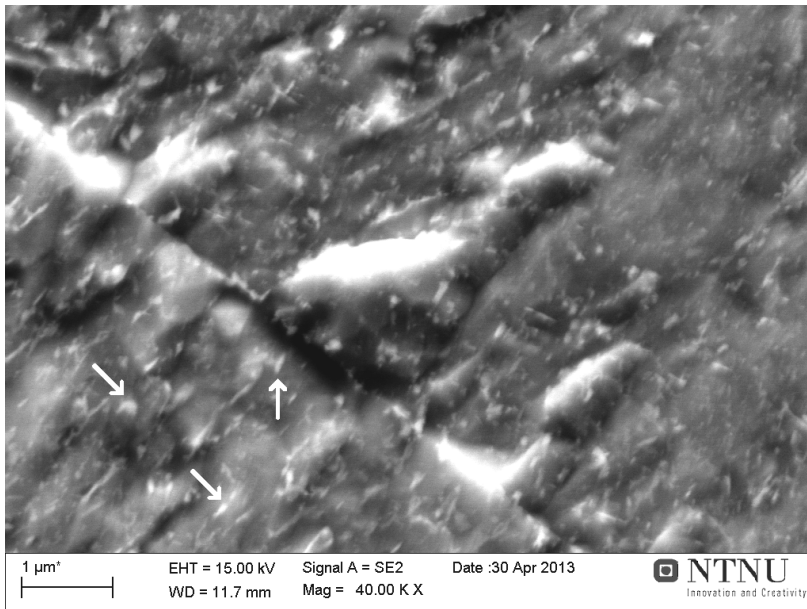


(b)

Figure 24: Comparison of the same spot in the microstructure imaged with both SEM and light microscope. The image from the light microscope has been inverted, cropped and digitally enlarged in order to accentuate that both image the same grain boundary. Sample imaged has been tempered for 7 minutes at 600° C. Note how the dark spots looking like carbides in the light microscope are in reality pits on the sample surface as revealed by the SEM image.



(a)

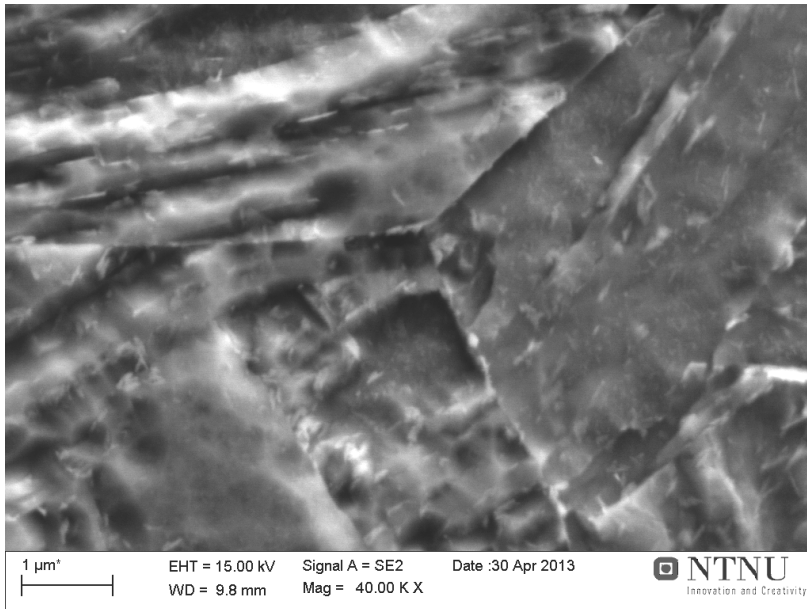


(b)

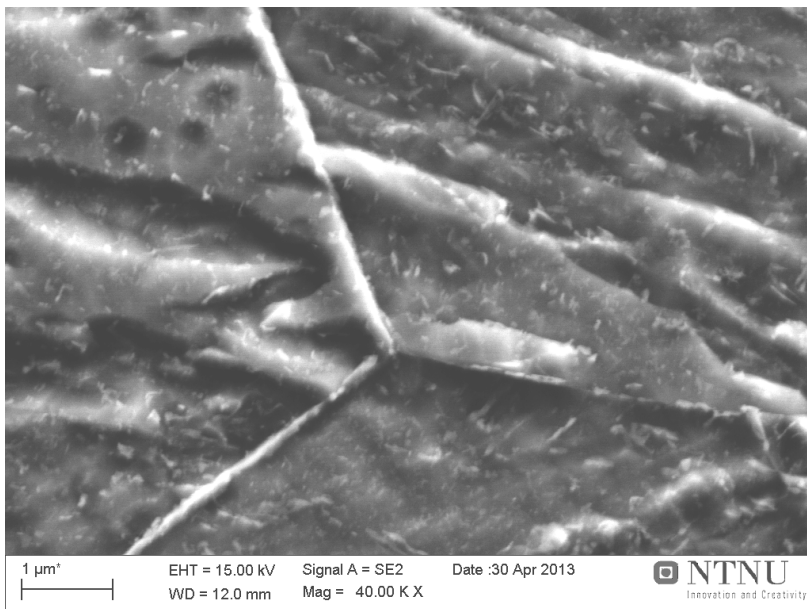
Figure 25: Microstructure of quenched and tempered samples imaged with secondary electron detector:

a) Tempered at 600°C for 7 minutes. Examples of lath-shaped carbides are indicated by arrows. Typical length: $0.2\ \mu\text{m}$. Typical width: $0.05\ \mu\text{m}$.

b) Tempered at 600°C for 48 hours. Examples of carbides are indicated by arrows. Note the precipitation and spheroidization, but still limited growth of carbides. Typical length: $0.2\ \mu\text{m}$. Typical width: $0.09\ \mu\text{m}$.



(a)



(b)

Figure 26: Microstructure of quenched and tempered samples imaged with secondary electron detector:

a) Tempered at 650°C for 5 minutes.

b) Tempered at 650°C for 3 hours. Note the precipitation and spheroidization, but still limited growth of carbides.

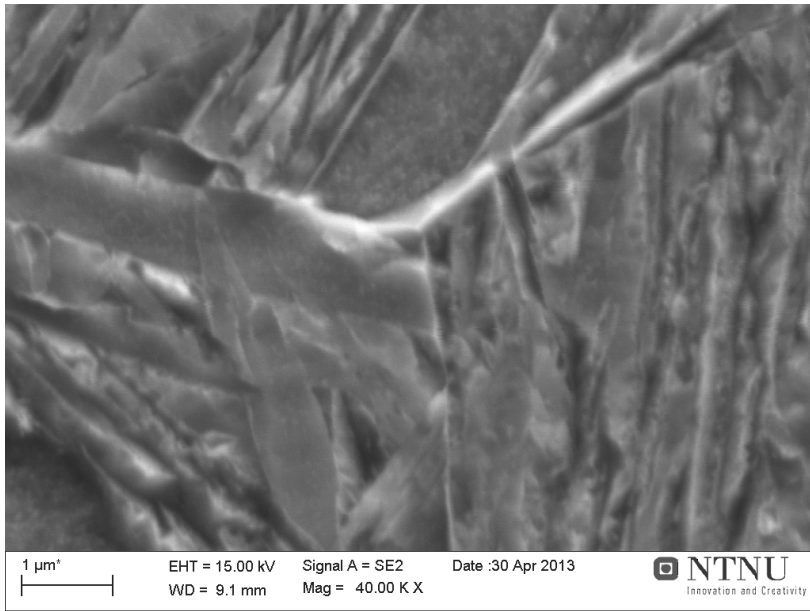
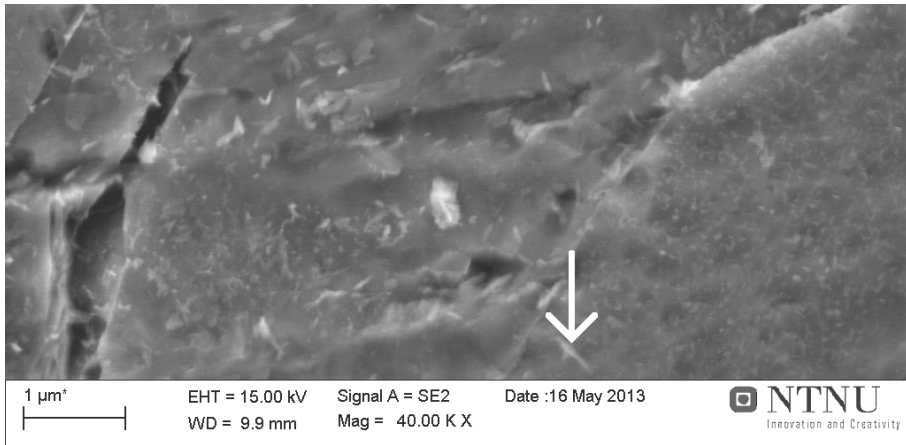
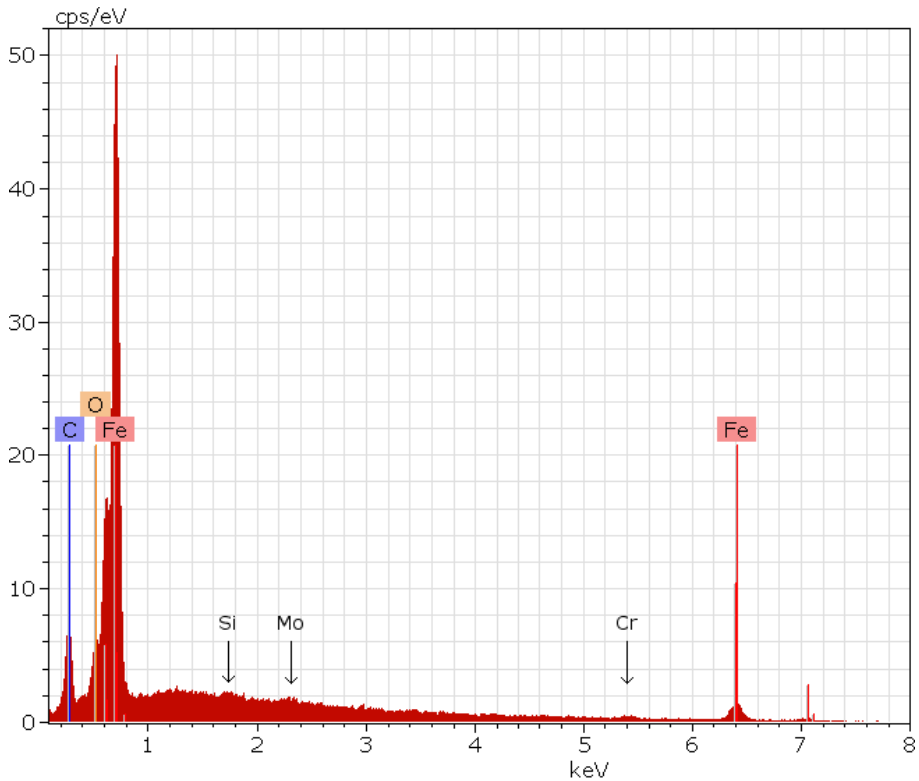


Figure 27: *As-quenched microstructure. When compared to the microstructures shown in Figures 25 and 26, the lack of carbides becomes evident.*

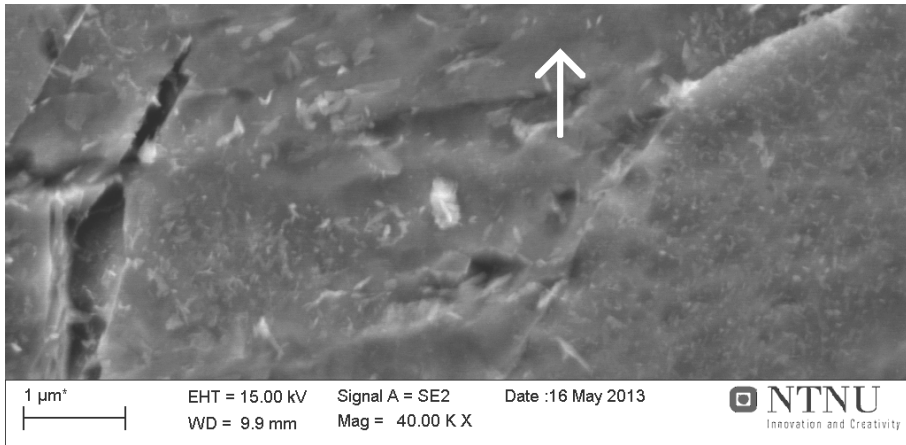


(a)

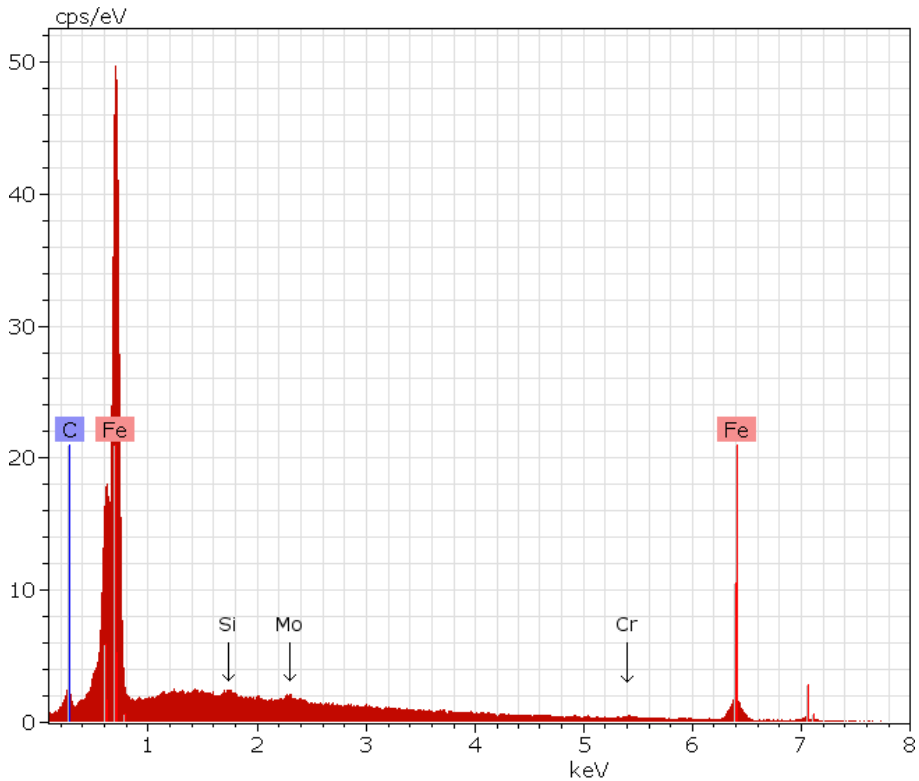


(b)

Figure 28: Results from EDS analysis of sample tempered for 7 minutes at 600°C :
 a) Image of analysed carbide. Arrow marks point of analysis.
 b) EDS spectrum from analysed carbide. Small “bumps” in the background radiation indicate the presence of Cr, Mo and Si.

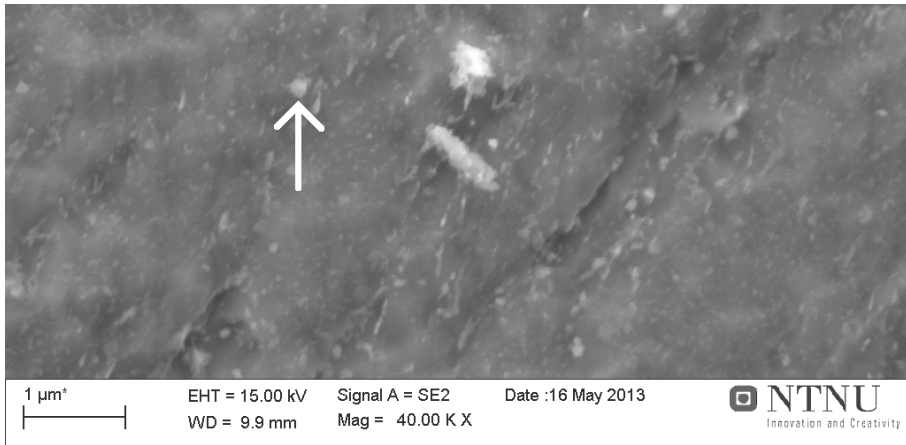


(a)

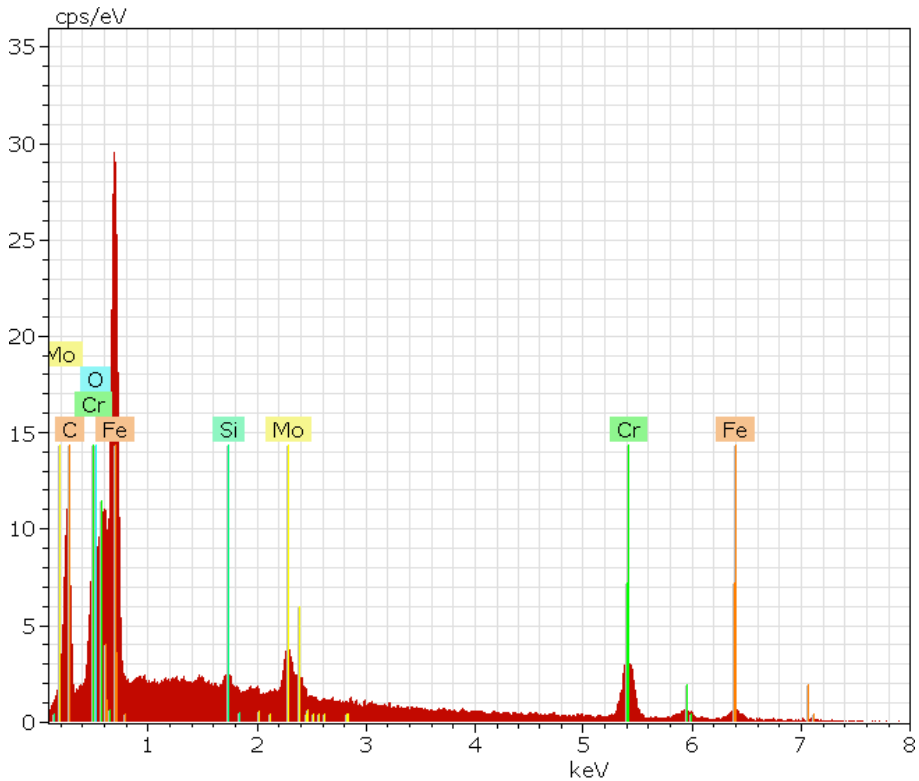


(b)

Figure 29: Results from EDS analysis of sample tempered for 7 minutes at 600°C:
 a) Image of analysed point. Arrow marks point of analysis. Only matrix has been analysed.
 b) EDS spectrum from matrix. Small “bumps” in the background radiation indicate the presence of Cr, Mo and Si.

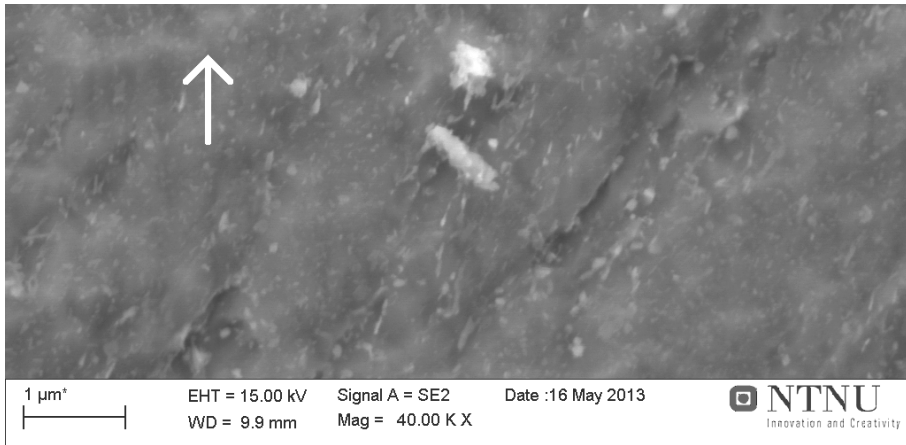


(a)

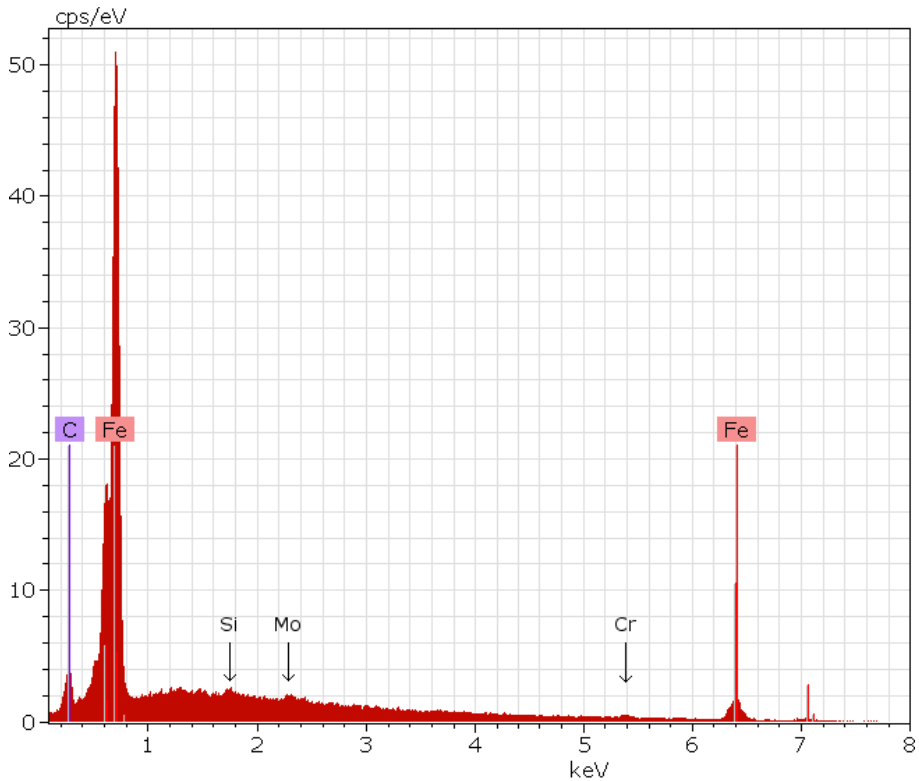


(b)

Figure 30: Results from EDS analysis of sample tempered for 48 hours at 600° C:
 a) Image of analysed carbide. Arrow marks point of analysis.
 b) EDS spectrum from analysed carbide. Note that the y-axis is scaled different from the other spectra.



(a)



(b)

Figure 31: Results from EDS analysis of sample tempered for 48 hours at 600° C:
 a) Image of analysed point. Arrow marks point of analysis. Only matrix has been analysed.
 b) EDS spectrum from matrix. Small “bumps” in the background radiation indicate the presence of Cr, Mo and Si.

4.2.3. Validity of the Hollomon-Jaffe relationship for F22 steel

During the quench and temper heat treatment, the tempering times were adjusted according to the Hollomon-Jaffe tempering relationship to see if the samples would obtain the same hardness and strength reduction when their tempering cycles produced the same Hollomon-Jaffe parameter, z .

Hardness was measured as 24 indentations on the two specimens making out a parallel couple.

Figure 32 shows the obtained hardness after having subjected the specimens to quenching and tempering. The tempering cycles were adjusted according to the Hollomon-Jaffe relation to produce paired samples having been submitted to equal tempering effects. This should produce five sample sets having equal hardness within each tempering set.

For the longer tempering times at 650°C (1 and 3 h), Hollomon-Jaffe was applied in analytical shape to determine the necessary tempering time for equal hardness reduction when tempering at 600°C. The samples tempered for 5, 10 and 30 minutes did not reach 650°C, so a numerical approach was used. Based on measurements of heating rate, shown in Appendix A.8 (p. 81), the trapezoidal method was used with step length $h=15$ seconds to produce paired samples.

Figure 32 shows fairly equal hardness values for the two different tempering temperatures at the different tempering levels, meaning that both the analytical solution of Hollomon-Jaffe at long tempering times and the numerical approach at shorter tempering times provided good results for the tempering effect of F22.

The reductions in yield and tensile strength from tempering are shown in Figure 33. Both the yield and the tensile stress follow the main trends shown in Figure 32, but it becomes clear that the tensile strength is more closely related to the hardness of the material than the yield strength.

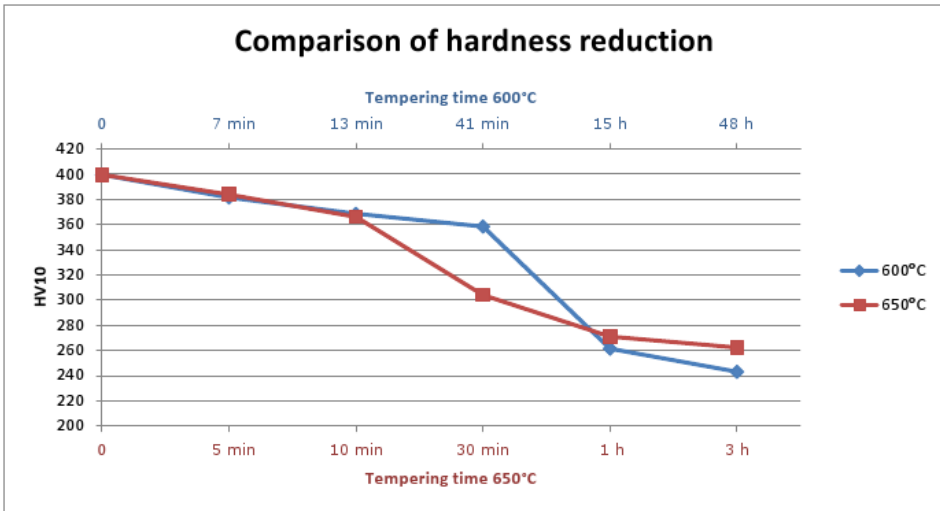
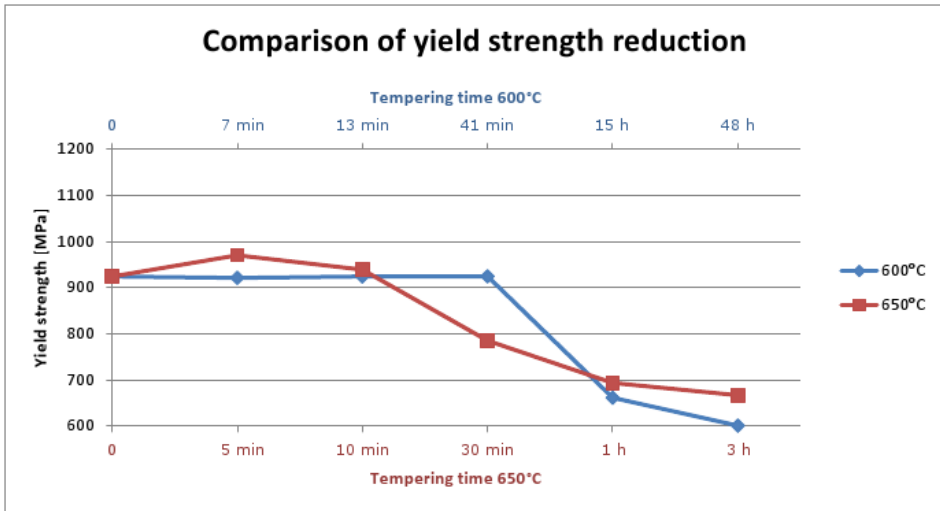
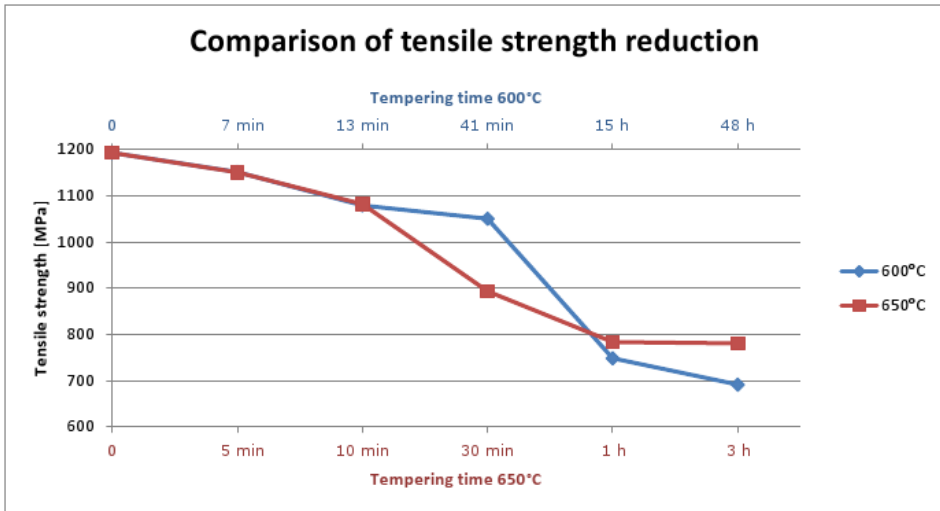


Figure 32: Graphic presentation of hardness reduction at equal tempering parameters for quenched and tempered material. There are two x-axes with different scaling in order to better compare the hardness reduction.



(a)



(b)

Figure 33: Graphic presentations of reduction of yield and tensile strength at equal tempering parameters for quenched and tempered material. Both figures contain two x-axes with different scaling, but where the tempering parameters are equal for the same physical x-location:

- a) Comparison of yield strength reduction.
- b) Comparison of tensile strength reduction.

4.2.4. Strength-hardness relations

In order to obtain a general correlation between strength and hardness, all tensile results, from the previous work [12], as well as the results for the weld simulated material and the quenched and tempered and controlled cooled tensile specimens from the present work have been utilized to establish a relation. This sums up to a total of 61 tensile specimens.

Tensile curves from tensile testing are shown in Appendices A.11 and A.12 (pp. 84–85), and a table containing the strength results from the tensile testing is given in Appendix A.10 (p. 83). All results regarding strength are calculated as nominal stress, and the abbreviations used are according to NS-EN 10002-1, as shown in Appendix A.2 (p. 76).

The hardness was calculated as an average of 12 indentations on each tensile specimen, a total of 732 indentations divided between 61 tensile specimens. The results are shown in Figures 34 and 35, where respectively yield and tensile strength have been plotted versus hardness for each tensile specimen.

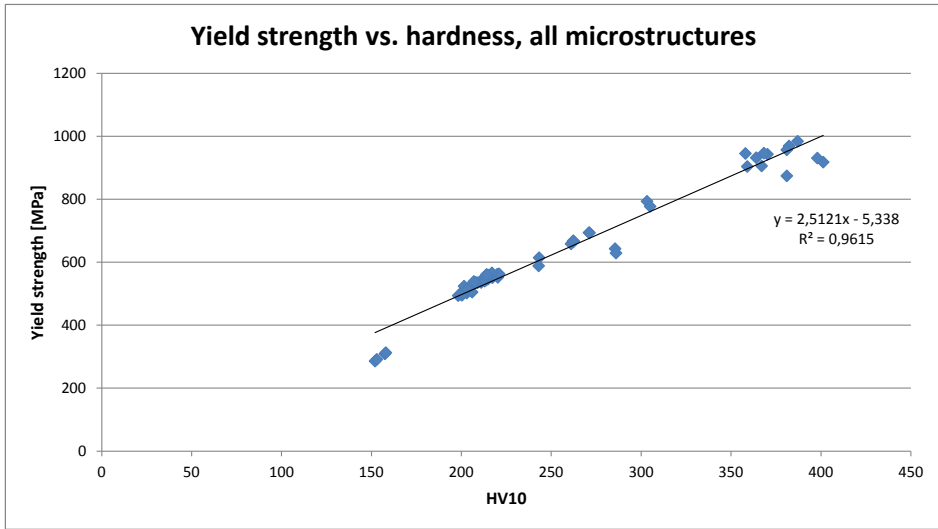
The hardness measurements of the tensile specimens were analysed statistically in order to ensure reliability of the results. The statistics revealed the following:

- The average, normalized percentage standard deviation, σ_N , was 2.2 %.
- The minimum and maximum values of σ_N were respectively 1.0 and 8.6 %. The largest deviations were measured in the samples having been cooled in the furnace, where the coarse grained ferrite-pearlite structure explains the variations in hardness.

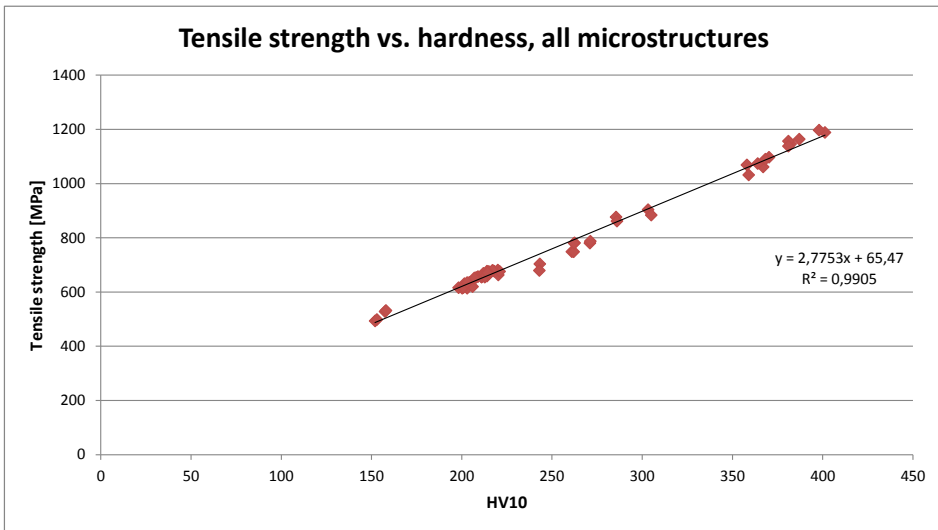
The regression equations shown in Figures 34 and 35 contain too many digits when compared to the uncertainty of the regressions. Because of this, they have been simplified and are shown together with their standard deviations in Table 9.

Table 9: *The new strength-hardness correlations for F22 steel with standard deviations, σ .*

Microstructure	Regression equation	σ [MPa]	Validity range [HV]
All	$R_{p0.2} = 2.51 \cdot HV - 6$	35	152–401
	$R_m = 2.78 \cdot HV + 64$	19	152–401
Martensite	$R_{p0.2} = 2.39 \cdot HV + 33$	22	198–401
	$R_m = 2.80 \cdot HV + 56$	19	198–401
Ferrite-pearlite	$R_{p0.2} = 2.58 \cdot HV - 101$	7	152–286
	$R_m = 2.74 \cdot HV + 87$	12	152–286



(a)

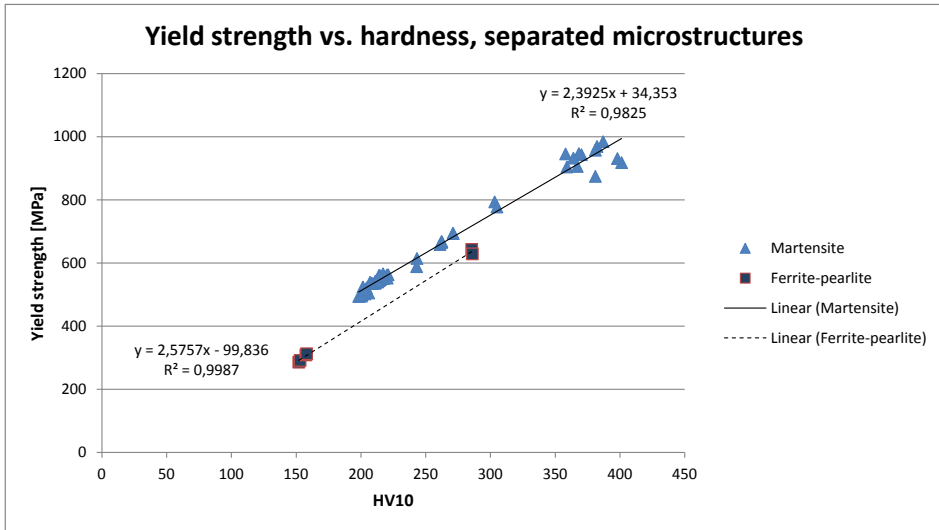


(b)

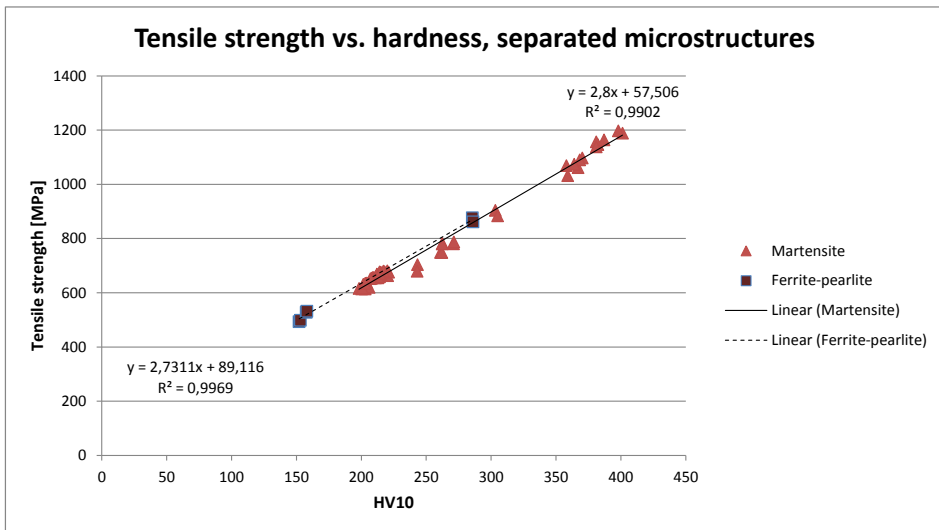
Figure 34: Data points and regression lines from measurements of strength and hardness of tensile specimens. Equations and R^2 -values for the regression lines are shown in the respective figures:

a) Yield strength plotted as a function of hardness for all tensile specimens.

b) Tensile strength plotted as a function of hardness for all tensile specimens.



(a)



(b)

Figure 35: Same data points as shown in Figure 34, but with the different microstructures separated in order to increase the precision of the regressions. Equations and R^2 -values for the regression lines are shown in the respective figures:
a) Yield strength plotted as a function of hardness for martensite and ferrite-pearlite specimens with trendlines separated according to microstructure.
b) Tensile strength plotted as a function of hardness for martensite and ferrite-pearlite specimens with trendlines separated according to microstructure.

4.2.5. Comparison with previous strength-hardness relations

In order to see if the strength-hardness relations shown in Section 4.2.4 are an improvement compared to prior relations, a comparison was performed for a selection of samples including both martensitic and ferrite-pearlite microstructures.

A comparison with the relations determined by Tabor [14] and Cahoon et al. [15, 16] required that the strain hardening coefficients associated with the various heat treatments had to be determined. This was done for a representative selection of specimens using Equation 6 (p. 14), and the results are presented in Table 10.

Cahoon et al. [15] calculated n from plots of $\ln \sigma$ versus $\ln \epsilon$. This was tried for a selection of tensile specimens, but a straight line was not obtained with Equation 5 (p. 14) for any of the specimens. In order to obtain a straight line, the Ludwik equation (p. 14) had to be applied, but this would still not produce results comparable to those obtained by Cahoon et al., who had used Equation 5, so the use of Equation 6 (p. 14) was considered a decent compromise.

The selected microstructures for the comparison varied from as-quenched to ferrite-pearlite structures. Because of this, the regressions used in the comparison had to be valid for several different microstructures. The expressions by Tabor, Cahoon and Cahoon et al. had no problems with this, since they are valid not just for all microstructures in steel, but even for other metals. On the other hand, the regressions determined by Pavlina and Van Tyne, as well as the new model presented in Section 4.2.4 (p. 54) would be more precise if applied for their respective microstructures. The comparison is therefore a “worst case study” for the linear expressions.

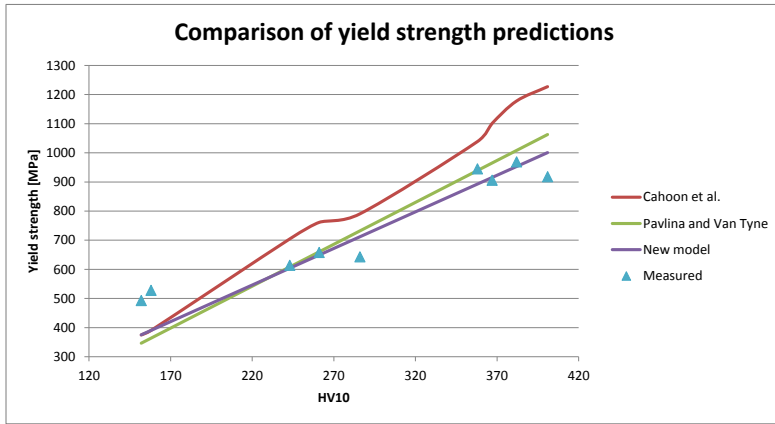
Figure 36 shows the results from the comparison. The standard deviations belonging to the different models are shown in Table 11. It is important to note that the standard deviations of the new model differ from those presented in Table 9 (p. 54), due to fewer data points evaluated, as well points fitting less with the model (“worst case study”).

Table 10: *The strain hardening coefficient, n , calculated for a selection of heat treatments.*

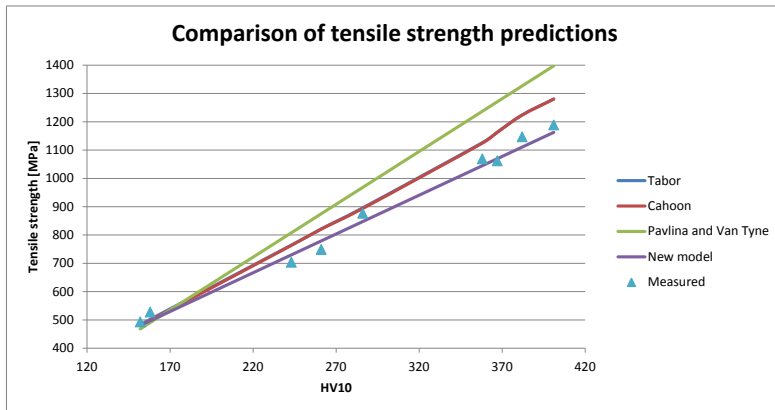
Heat treatment	n
Q	0.029
Q + T: 600°C, 7 min	0.025
Q + T: 600°C, 13 min	0.037
Q + T: 600°C, 41 min	0.052
Q + T: 600°C, 15 h	0.050
Q + T: 600°C, 48 h	0.052
IT: 600°, 30 h	0.073
IT: 700°, 6 h	0.123
Furnace cooled	0.122

Table 11: Comparison of standard deviations calculated for the different models according to Equation 13 (p. 26).

Model	$\sigma_{R_{p0.2}}$ [MPa]	σ_{R_m} [MPa]
Tabor	-	73
Cahoon	-	73
Cahoon et al.	193	-
Pavlina and Van Tyne	108	162
New model	82	30



(a)



(b)

Figure 36: Graphic comparison of the different strength-hardness correlations for a selection of samples. Models valid for all microstructures were used:
 a) Comparison between calculated and measured yield strength.
 b) Comparison between calculated and measured tensile strength. Results calculated with the expressions by Tabor and Cahoon overlap almost completely.

5. Discussion

5.1. Weld simulation investigations

5.1.1. Weld hardness profiles

The weld hardness profiles obtained the expected shape, with increased hardness in the HAZ, when compared to the hardness of the base material. This is caused by the formation of martensite and bainite in the HAZ during weld simulation, as examined during the previous investigations [12].

Tempering led to softening of the HAZ. This is mainly caused by annihilation of dislocations and precipitation of carbides, relieving lattice stresses. At longer tempering times (more than 1 hour) the Ostwald ripening effect will lead to coarsening and spheroidization of cementite particles at martensite lath boundaries as reported by Speich [27] as well as by Caron and Krauss [28]. The later authors reported that Fe-C martensite would start precipitation of carbon after just seconds of tempering.

The microstructural investigations (see Sections 4.2.1, p. 35 and 4.2.2, p. 40) of quenched and tempered F22 steel revealed limited growth of carbides during tempering. This is believed to be caused by the presence of chromium and molybdenum. These elements form carbides, but due to their slow diffusion, they will not grow much, even during prolonged tempering. Initial precipitation of cementite was proven by SEM and EDS analysis, as well as the transition to chromium and molybdenum based carbides after prolonged tempering. The limited growth of carbides limits the softening of the steel, as they will act as dispersed precipitates in the microstructure.

The weld hardness profiles confirmed the expectations presented by the present author in the previous project [12]. From calculations based on Hollomon-Jaffe (Equation 2, p. 10), equal hardness reduction in material tempered for 2 hours at 650°C and in material tempered for 6 hours at 625°C was expected. These expectations were met when the samples tempered for 3 hours at 650°C had a greater loss of hardness than samples tempered for 6 hours at 625°C.

The Hollomon-Jaffe relation is expressed as $z = T(c + \log(t))$. This relation involves taking the logarithm of time, which reduces the significance of the time-value. The temperature, on the other hand, is a multiplying factor, and will thereby have a heavy impact on the tempering effect. As shown by the results from weld simulation investigations, this seems to be valid for the F22 steel, and is further supported by the results presented in Section 4.2.3 (p. 50), which will be discussed later.

With regards to requirements for mechanical properties, it becomes clear that it is easy to get the hardness below 275 HV as is required for the cap region of the weld. This was accomplished after just 1 hour of tempering at 650°C. The problem is that it is a lot harder to obtain further hardness reduction. The samples tempered

at 650°C for 6 hours were able to satisfy the 250 HV requirement, but the samples tempered for 3 hours at the same temperature were slightly above 250 HV in certain areas of the HAZ, thereby failing to satisfy the mechanical requirements.

5.1.2. Hardness development

Figure 19 (p. 32) shows the effect of tempering time and temperature on the hardness of weld simulated F22 steel specimens. The logarithmic x-axis partly distorts the large initial hardness reduction at shorter tempering times, but makes it clear that most of the softening occurs during the first hour of tempering.

One of the curves from the previous work [12], 10°C/s, 625°C, is almost flat during the first stages of tempering. The reason for this is not known, but a possible explanation could be secondary hardening. The presence of carbide forming elements like chromium and molybdenum makes the formation of dispersed alloy carbides plausible. Still, there is no observed effect like this in the 60°C/s, 625°C-curve. This makes secondary hardening unlikely, since a higher cooling rate should result in more dissolved chromium and molybdenum available for precipitation as alloy carbides during tempering. From these results, it seems that the horizontal part of the 10°C/s, 625°C-curve may be accredited to experimental deviations.

The results reveal that when tempering for 3 hours or more at temperatures above 600°C, the main tempering effect comes from the temperature, and is not very time dependent. This is in accordance with the results obtained by Murphy and Woodhead [29]. It also proves the validity of the Hollomon-Jaffe parameter (Equation 2, p. 10), where it can be seen that small variations in temperature will lead to substantial changes in tempering time if the same hardness reduction is to be achieved.

5.1.3. Tensile testing

Base material and untempered, weld simulated material Tensile testing of the base material and untempered, weld simulated material produced approximately the same results as predicted by the present author [12]. The base material proved slightly stronger than the samples tested in the previous work, where the samples had been weld simulated and tempered for 6 hours at 625°C. According to Hollomon-Jaffe, prolonged tempering of already heavily tempered material will only weaken the material slightly.

The weld simulated and untempered samples were tested as a reference to the effect of weld simulation on the strength of the material. All weld simulated samples subjected to tensile testing fractured in the base material, far outside the HAZ, and it was therefore believed that the same strength would be observed when comparing base material and weld simulated, untempered tensile samples. This seems to be correct, as the base material and weld simulated material exhibited similar strength, with the exception of the weld simulated sample subjected to a

cooling rate of 60°C/s. Both tensile specimens from this weld simulation sample fractured at the same “location”, and far outside the HAZ. The low strength is therefore believed to be caused by a material defect for these tensile specimens.

All tensile tests of untempered base material, revealed too low strength to satisfy the requirements for the F22 steel, as presented in Appendix A.1 (p. 75). The elongation values are not so relevant because some samples fractured close to the knife of the extensometer, resulting in lower elongation than what should have been recorded. In addition, the weld simulated samples elongate less during tensile testing due to strengthening of the HAZ from weld simulation. This effect can be observed in Figure 20 (p. 33).

Compared to the test results presented by the material certificate (Table 2, p. 18), the tensile testing revealed significantly weaker material, where both yield and tensile strength were more than 60 MPa lower. This could be caused by sample location, but the strength requirements are valid for all the material. Therefore, it seems that tested certificate values have not been representative for the supplied material.

Weld simulated and tempered material Tensile testing of weld simulated and tempered material produced much the same results as those obtained in the previous investigation of the F22 steel [12]. All fractures took place in base material. The tempering proved to have a certain effect on the strength, as can be seen from Table 7 (p. 34), where both yield and tensile strength decrease with increasing tempering time. Lower strength was expected when tempering at 650°C for 6 hours when compared to the results obtained in the previous work, where the same material was tempered at 625°C for 6 hours. This was not the case, and the most plausible explanation is variations in the supplied material. Still, the strength was in the same range, and none of the results were able to satisfy the requirements for yield and tensile strength.

The decrease in strength from increasing tempering time corresponds well with the Hollomon-Jaffe relation (Equation 2, p. 10). The increase in tempering effect is highest at short tempering times, but even during prolonged tempering, the Hollomon-Jaffe relation predicts softening and weakening of the material. This can be observed in Table 7 (p. 34), where the yield and tensile strength decrease as the tempering time increases.

Fractures occurring close to the knife of the extensometer, combined with reduced elongation due to a strengthened HAZ in weld simulated samples, result in elongation values that cannot be compared directly with the requirements for elongation. A possible solution to measure ductility is therefore to use the percentage area reduction, Z . When looking at Table 7 (p. 34), it seems that the area reduction is linked to the tempering of the material. This might be a coincidence, since the difference in area reduction is small. Increased tempering should increase the area reduction, but to which extent is not known. Investigating the link between area reduction and ductility could be a future field of study.

5.2. Strength-hardness relationship

5.2.1. Metallographic and SEM examination

Quenched and tempered samples The quench-temper heat treatments produced several interesting microstructures. The metallographic examination revealed that the F22 steel has a high hardenability. Even 20 mm thick samples turned martensitic when left to air cool after austenitizing. Even so, most of the martensitic samples contained some bainite. This was first observed in the previous investigation [12], in which a break in the cooling curves was observed at the calculated B_s temperature, which is higher than the calculated M_s .

Figures 21 (p. 37), 25, 26 and 27 (pp. 43–45) show the microstructures of quenched and tempered samples, as well as the as-quenched microstructure. The tempered microstructures are fairly similar in appearance, and the structures having gone through paired tempering procedures are almost identical in appearance. This seems promising with regards to the Hollomon-Jaffe relation (Equation 2, p. 10), which was used to determine the tempering time necessary for obtaining equal tempering effects when tempering at 600°C and 650°C.

The microstructures shown in Figures 25, 26 and 27 (pp. 43–45) illustrate the differences introduced by tempering. The as-quenched sample shown in Figure 27 contains no visible carbides. The structures tempered for 48 and 3 hours shown in Figures 25b) and 26b) respectively, contain small, slightly spheroidized, dispersed carbides. The slightly tempered structures shown in Figures 25a) and 26a) contain some very small, lath-shaped carbides and have been tempered for respectively 7 and 5 minutes.

The shape change of the carbides during prolonged tempering is in good agreement with existing theory. It is well known that cementite formed initially during tempering often can be lath-shaped. The presence of carbide forming elements such as chromium and molybdenum makes it plausible that alloy carbides form during tempering. According to the theory presented by Bhadeshia and Honeycombe [20, pp. 195–197], alloy carbides can form at the expense of cementite by dissolving the previously precipitated cementite particles, forming stable, dispersed alloy carbides. The slow diffusion of chromium and molybdenum keep these particles from growing into large inclusions through Ostwald ripening, which can explain their modest size even after 48 hours of tempering at 600°C, as shown by Figure 25b) (p. 43).

The formation of alloy carbides was supported by the EDS analysis, which indicated increased contents of chromium and molybdenum in the carbides having been tempered for 48 hours, while the carbides in sample tempered for 7 minutes did not differ much from the matrix with regards to chromium and molybdenum content. The observations match well with theory considering carbide formation. Measurements of core temperature during tempering revealed that the core of the sample tempered for 7 minutes reached approximately 425°C before the sample

was removed from the furnace, see Figure A.8 (p. 81). This means that the sample entered the optimal temperature region for formation of dispersed lath-shaped cementite, without reaching temperatures high enough to precipitate alloy carbides. The formation of carbides in this specimen has therefore been in good agreement with existing theory regarding tempering and formation of alloy carbides.

Ferrite-pearlite samples Controlled cooling and isothermal treatment produced three different microstructures with fascinating characteristics.

Figures 22a) and 23a) (pp. 38–39) both show a sample allowed to cool in the furnace from 1200°C down to ambient temperature. This process produced the expected coarse grained ferrite-pearlite microstructure, the coarse grains being caused by the long time at high temperatures (900-1200°C). Most of the pearlite has been transformed during cooling, which has resulted in what is believed to be degenerated pearlite, but traces of the lamellar structure can still be observed.

Figures 22b) and 23b) (pp. 38–39) show a ferrite-pearlite structure obtained by austenitizing, followed by isothermal treatment at 700° for 6 hours. The microstructure is a mixture of ferrite, pearlite and martensite. As shown in Table 8 (p. 36), the pearlite has been separated in coarse and fine pearlite. The higher hardness of the fine pearlite is caused by its increased surface area, which provides a strengthening contribution. It is evident that the transformation to ferrite-pearlite was not complete, since grains of martensite are observed throughout the structure. These grains were probably carbon enriched retained austenite which transformed to martensite when the sample was left to cool in air to ambient temperature. During isotherm transformation, alloying elements have been accumulated in retained austenite grains by diffusion. This has probably displaced the curves of the IT-diagram, according to the theory presented in Section 2.6, p 11, leading to longer transformation times, which eventually resulted in the formation of martensite during air cooling to ambient temperature.

The sample shown in Figures 22c) and 23c) (pp. 38–39) contains a mixed microstructure. Grain boundary allotriomorphs are easily distinguished along with some Widmanstätten ferrite, intragranular idiomorphs and intragranular plates (can be seen in the upper left and centre of Figure 22c)). The main phase of the sample contains a complex structure, which is believed to be degenerated pearlite. Bhadeshia and Honeycombe have presented the effects of alloying elements on the structure of pearlite [20, pp.80–91]. It is from their explanation possible that the strong presence of carbide forming elements such as chromium and molybdenum could be the explanation for the strange microstructure observed in Figure 22c) and 23c). The hardness of the strange structure could point to pearlite, bainite or tempered martensite, but the similarities, both with respect to visual character and hardness, with the pearlite of the furnace cooled sample are in favour of the structure being degenerated pearlite. The low transformation temperature is believed to be the cause of the large area fraction pearlite, and this is also in accordance with the hardness being lower than that of the degenerated pearlite in the furnace

cooled sample, since a larger area fraction pearlite would mean a larger fraction soft ferrite in the degenerated pearlite.

The microhardness measurements of the degenerated pearlites revealed a fairly hard microstructure (see Table 8, p. 36). Despite being higher than the hardness usually found in pearlite, this is still in accordance with results presented by Karlsson and Lindén [38], who observed even higher hardness in work hardened pearlite than the results presented in this thesis. Both the fine and coarse pearlite in the sample transformed isothermally at 700°C is significantly softer than the degenerated pearlites in the samples subjected to furnace cooling and isothermal heat treatment at 600°C. The explanation behind the large difference between the hardness of the different pearlites is not known.

5.2.2. Validity of the Hollomon-Jaffe relationship for F22 steel

Figure 32 (p. 52) shows the hardness development during tempering of samples where the tempering cycles have been adapted to produce paired samples with equal Hollomon-Jaffe parameters, despite having been tempered at different temperatures. A decent match in hardness was obtained for most sample pairs, even though the tempering parameter had been calculated with different methods.

A difference in hardness can be observed for the samples tempered for 30 and 41 minutes. The Hollomon-Jaffe relation is a very temperature dependent relation, making small variations in time insignificant, while small variations in temperature have significant effects on the tempering effect. When looking at the heating curves shown in Appendix A.8 (p. 81), it seems that both specimens reached a temperature very close to the programmed tempering temperature, and were kept there for a short amount of time (≈ 10 minutes). This means that the specimen tempered for 41 minutes at 600°C probably should have been tempered for approximately 2 hours and 15 minutes (calculated from an analytical solution of Hollomon-Jaffe for 10 minutes of tempering at 650°C) in order to obtain the same hardness as that of the sample tempered for 30 minutes at 650°C.

The results shown in Figure 33 (p. 53) show that there is a close connection between strength and hardness. The development of strength follows the development of hardness during tempering.

When comparing the results shown in Figures 32 and 33 (pp. 52–53), it becomes evident that the tensile strength is more closely related to hardness than the yield strength. This was expected, since hardness measurements are based on plastic deformation of the material. A correlation between tensile strength and hardness will both take plastic deformation and the accompanying work hardening into account, while the yield strength is dependent on other factors like grain size, precipitate hardening and initial dislocation density.

Another interesting observation is that the yield strength is seemingly unaffected by the first stages of tempering. The reason for this is not understood. It could

be caused by experimental deviations. Another possible explanation is that the precipitation of carbon as lath shaped ϵ -carbide or cementite could produce a strengthening contribution, or secondary hardening. This strengthening could then level out the softening effect from a reduction of carbon in solid solution and annihilation of dislocations. This is supported by the SEM and EDS investigation, where lath-shaped, iron-based carbides were observed. On the other hand, the carbides observed in the SEM for the shorter tempering times, see Figures 25 and 26 (pp. 43–44) were not very densely distributed, so they should not give much of a hardening contribution. It is important to note that secondary hardening is a possible explanation, and not a verified result.

5.2.3. Strength-hardness relations

The new strength-hardness relations for the F22 steel are presented in Table 9 (p. 54). In order to increase the precision of the models, a separation based on microstructure has been done. Different regressions have been made for ferrite-pearlite and martensitic microstructures.

The universal regression for tensile strength, including both microstructures, proved to be a good match with the experimental results, and no significant reduction in standard deviation was obtained by splitting into separate regressions for the different microstructures.

This result contradicts the findings of Pavlina and Van Tyne, who found it hard to establish a precise, linear regression for tensile strength. Their explanation was that other material properties, like the strain hardening coefficient, had to be taken into account to produce a more precise expression. This is probably caused by their work being of a more general character, where more than 150 different steels were examined without taking their different response to deformation into account.

The new expression is, on the other hand, based entirely on tests performed with the F22 steel, making the new model applicable only for the F22 alloy specification. The advantage is that it is much more precise when used within its validity range.

It proved to be more difficult to establish a precise relation for yield strength, which is less connected to the hardness of the material. For the yield strength, dividing between the different microstructures produced better regressions with lower standard deviations.

5.2.4. Comparison with previous strength-hardness relations

The comparison of different strength-hardness relations provided several interesting results. The tensile strengths calculated with the expressions derived by Tabor [14] and Cahoon [16] overlapped almost completely, making these two expressions equivalent with regard to both precision and deviations.

When comparing Figures 36a) and 36b) (p. 58), it becomes clear that an approximation of the yield strength is generally less precise than an approximation of the tensile strength. The main reason is that measurement of hardness and tensile strength both include plastic deformation, leading to more direct comparison of material properties.

Estimation of yield strength based on hardness measurements proved to be a more difficult task, but the linear regression by Pavlina and Van Tyne proved surprisingly precise, especially when regarding its wide background and broad validity range. Still, the smallest standard deviation was calculated for the new model, with $\sigma = 82$ MPa, a result 26 MPa better than the standard deviation for the model by Pavlina and Van Tyne. The model developed by Cahoon et al. had an extremely high standard deviation of 193 MPa, making it almost useless for practical use.

When it came to the tensile approximations, the model by Pavlina and Van Tyne proved to be useless with a standard deviation of 162 MPa, while the older expressions by Tabor and Cahoon gave better approximations with $\sigma = 73$ MPa. The best approximation was once again by the new model, with a standard deviation of 30 MPa. It seems from these results that the bulk hardness will not provide enough of the material properties for approximating tensile strength. The precision of the models by Tabor and Cahoon makes it plausible that work hardening plays a major role in the link between hardness and tensile strength. This will in turn make estimates for tensile strength less accurate if they are based entirely on bulk hardness and generalized for different materials.

6. Conclusion

F22 steel has been heat treated, tested mechanically and subjected to microstructural investigations. The concluding remarks can be summarized as follows:

- The investigated F22 steel did not satisfy the requirements to strength according to the FMC specifications, M20717. Thereby, the strength was also lower than the strength presented by the material certificate which followed the steel.
- Increased tempering temperature increases the tempering effect significantly. The Hollomon-Jaffe tempering relationship proved valid for calculation of tempering effect in F22 steel.
- The performed weld simulation did not affect the strength of the material, as fracture took place in the unaffected base material for all tensile specimens.
- The following relations between strength and hardness of F22 were found to produce good estimates for strength:
 - Yield strength of martensitic microstructures:
 $R_{p0.2} = 2.39 \cdot HV + 33, \sigma = 22 \text{ MPa}.$
 - Yield strength of ferrite-pearlite microstructures:
 $R_{p0.2} = 2.58 \cdot HV - 101, \sigma = 7 \text{ MPa}.$
 - Tensile strength, valid for all microstructures:
 $R_m = 2.78 \cdot HV + 64, \sigma = 19 \text{ MPa}.$
- Compared to previously developed strength-hardness relations, the new model proved more accurate for approximating yield and tensile strength of the F22 steel. How the new model behaves for other steel qualities has not been tested.
- Hardness measurements give a good basis for approximating tensile strength. Yield strength can also be approximated from hardness measurements, but not as precisely.
- A linear regression between tensile strength and hardness will only be precise when developed for a specific material, due to individual strain hardening rates.

7. Further work

A master's work like this, looking at so many different aspects of F22 steel, opens the door for a multitude of further investigations.

A more thorough investigation of microstructural development during tempering is a possible way to continue the investigations of F22 steel. More advanced techniques could be used to precisely determine the phase composition of the carbides present after tempering of F22 steel. EDS in TEM is one possibility. Another option is the Replica technique, where carbides are bonded to a polymer film and removed from the steel before being investigated with EDS in the SEM or TEM. This could be done for samples subjected to both different tempering times and temperatures, in order to determine the type, and effect, of carbides precipitating during tempering.

The degenerate pearlite structure obtained from isothermal heat treatment at 600°C for 30 hours exhibited interesting properties with regards to strength. It could therefore be of interest to reproduce this microstructure, determine how easily it forms, and to further test its mechanical properties. Pearlite structures are often avoided in offshore applications due to poor impact toughness. Testing of strength, hardness and impact toughness would therefore be of interest to see if the degenerate pearlite structure could be applicable for engineering purposes.

During this master's work, no heat treatments have been performed in order to produce bainite. This microstructure is often considered beneficial due to good mechanical properties, at least for lower bainite. It could therefore be of interest to heat treat in order to obtain bainite, followed by testing to compare its mechanical properties to those of the microstructures investigated in this master's work.

When performing tensile tests of weld simulated material where both the HAZ and unaffected base material are within the parallel area of the tensile specimen, it is misleading to use the obtained elongation value to describe ductility. Tensile testing of weld simulated material indicated that area reduction could prove a more reliable connection to ductility. In order to see if this is a useful connection, further investigations relating area reduction to the ductility of the material is needed.

When it comes to strength-hardness relations for F22 steel, further experimental background could always be of interest to increase the certainty of the predicted yield or tensile strength. However, for the testing of as-delivered F22, 25 tensile specimens have been tested as base material or weld simulated material. These have given a decent background for the hardness and strength range expected in as-delivered F22. This means that further investigations should rather focus on ferrite-pearlite or less tempered martensitic or bainitic microstructures in order to contribute to new knowledge of the strength and hardness of F22 steel.

References

- [1] Yong Bai, R. Bhattacharyya, and M.E. McCormick. Chapter 20: Design of deepwater risers. In *Pipelines and Risers*, volume 3 of *Elsevier Ocean Engineering Series*, pages 381 – 392. Elsevier, 2001. doi: 10.1016/S1571-9952(01)80034-9. URL <http://www.sciencedirect.com/science/article/pii/S1571995201800349>.
- [2] FMC Technologies. Riser Illustration. <http://www.fmctechnologies.com/en/SubseaSystems/Technologies/AdvancingTechnologies/Intervention/LS.aspx>, 2012.
- [3] P.T. Moe, B. Salberg, K. Rabben, B. Halmrast, J.I. Audestad, J.S. Burnell-Gray, and W. Rudd. Shielded Active Gas Forge Welding - From Laboratory to Field Experiments. *International Journal of Material Forming*, 3(1):1027–1030, 2010.
- [4] Morten Ro Helsem. Controlled cooling during forge welding. Technical report, 2008.
- [5] Morten Ro Helsem. Thermal cycles applied on the medium carbon steel J55. Master’s thesis, NTNU, 2009.
- [6] Ørjan Aronsen Ellingsen. The effect of tempering and normalizing on steel alloy L80. Technical report, 2009.
- [7] Ørjan Aronsen Ellingsen. Forge welding of the non-weldable steel qualities K55, L80 and L80SS. Master’s thesis, NTNU, 2010.
- [8] Ruth Oftedal Herikstad. Forge welding and weld simulations on a J55 steel. Technical report, 2010.
- [9] Ruth Oftedal Herikstad. Thermal Forge Welding Simulations. Master’s thesis, NTNU, 2011.
- [10] Erlend Sølvsberg. Properties and microstructures in X80 after weld simulation. Technical report, 2011.
- [11] Aleksander Rudolf Stoss. SAG-FW Welding of C90 Riser Steel Connectors. Master’s thesis, NTNU, 2012.
- [12] Trond Arne Hassel. Thermal Forge Welding Simulations of F22 Steel. Technical report, 2012.
- [13] E.J. Pavlina and C.J. Van Tyne. Correlation of Yield Strength and Tensile Strength with Hardness for Steels. *Journal of Materials Engineering and Performance*, 17(6):888–893, 2008.
- [14] D. Tabor. The Hardness and Strength of Metals. *Journal of the Institute of Metals*, 79:1–18, 1951.

- [15] J.R. Cahoon, W.H. Broughton, and A.R. Kutzak. The Determination of Yield Strength From Hardness Measurements. *Metallurgical Transactions*, 2:1979–1983, July 1971.
- [16] J.R. Cahoon. An Improved Equation Relating Hardness to Ultimate Strength. *Metallurgical Transactions*, 3:3040, November 1972.
- [17] M.J. Marcinkowski, R.M. Fisher, and A. Szirmae. Effect of 500°C Aging on the Deformation Behavior of an Iron-Chromium Alloy. *Metallurgical Transactions*, 230:676–689, 1964.
- [18] G.R. Speich and H. Warlimont. Yield Strength and Transformation Substructure of Low-Carbon Martensite. *The Journal of the Iron and Steel Institute*, 206:385–392, 1968.
- [19] K. Yagi. 2.25Cr-1Mo steel. In *Creep Properties of Heat Resistant Steels and Superalloys*, pages 67–73. Springer, 2004.
- [20] H.K.D.H. Bhadeshia and R.W.K. Honeycombe. *Steels: Microstructure and Properties*. Butterworth-Heinemann, 2006.
- [21] B.E. Sundquist. The Edgewise Growth of Pearlite. *Acta Metallurgica*, 16:1413–1427, 1968.
- [22] H.K.D.H. Bhadeshia and J.W. Christian. Bainite in Steels. *Metallurgical Transactions*, 21A:767–797, 1990.
- [23] G.R. Speich and W.C. Leslie. Tempering of Steel. *Metallurgical Transactions*, 3(5):1043–1054, 1972.
- [24] G.F. Vander Voort, editor. *Atlas of Time-Temperature Diagrams for Irons and Steels*. ASM International, 1991.
- [25] J.H. Hollomon and L.D. Jaffe. Time-temperature Relations in Tempering Steel. *Metallurgical Transactions*, 162:223–249, 1945.
- [26] V.H. Baltazar Hernandez, S.S. Nayak, and Y. Zhou. Tempering of Martensite in Dual-Phase Steels and Its Effects on Softening Behaviour. *Metallurgical and Materials Transactions A*, 42A:3115–3129, October 2011.
- [27] G.R. Speich. Tempering of Low-Carbon Martensite. *Metallurgical Transactions*, 245:2553–2564, 1969.
- [28] R.N. Caron and G. Krauss. The Tempering of Fe-C Lath Martensite. *Metallurgical Transactions*, 3:2381–2389, September 1972.
- [29] S. Murphy and J.H. Woodhead. An Investigation of the Validity of Certain Tempering Parameters. *Metallurgical Transactions*, 3:727–735, March 1972.
- [30] S.L. Semiatin, D.E. Stutz, and T.G. Byrer. Induction Tempering of Steel: Part I. Development of an Effective Tempering Parameter. *American Society for Metals*, 4(1):39–46, June 1985.

- [31] Irving and Pickering. *Journal of the Iron and Steel Institute*, 194:137, 1960.
- [32] Kinsman and Aaronson. *Transformation and Hardenability in Steels*. Climax Molybdenum Co., Michigan, USA, 1967.
- [33] P.H. Moe. *Sammenføyningsmetoder ved rørlegging til havs*. PhD thesis, NTH, 1986.
- [34] G.E. Dieter. *Mechanical Metallurgy*. McGraw-Hill Book Co, Singapore, 1998.
- [35] Ivan Samardžić and Marko Dunder. Contribution to Weldability Investigation of Steel TStE 420 on Welding Thermal Cycle Simulator. R. Cebalo & H. Schultz Ed., 2002. 8th International Scientific Conference on Production Engineering – CIM'2002.
- [36] R.H. Myers, S.L. Myers, R.E. Walpole, and Keying Ye. *Probability & Statistics for Engineers & Scientists*. Pearson Education International, 2007.
- [37] J. Hjelen. *Scanning elektron-mikroskopi*. Metallurgisk institutt, NTH, 1989.
- [38] B. Karlsson and G. Lindén. Plastic Deformation of Ferrite – Pearlite Structures in Steel. *Materials Science and Engineering*, 17(2):209–219, 1975.

A. Appendix

Figure A.1: *Requirements for mechanical properties. Test procedures stated in ISO 148-1 and NS EN ISO 6892. Requirements are according to ISO 13628-7 with the exception of strength, where FMC have provided the requirement based on engineering applications. These requirements are stated in FMC's internal guidelines, M20717. The strength requirements were originally given as 85 and 100 ksi, which explains the strangely precise strength requirements in MPa. Hardness is to be measured as close to fusion line as possible and 1.5-2 mm below surface. Provided by Svein Bratterud, FMC Technologies. As shown in the previous work [12].*

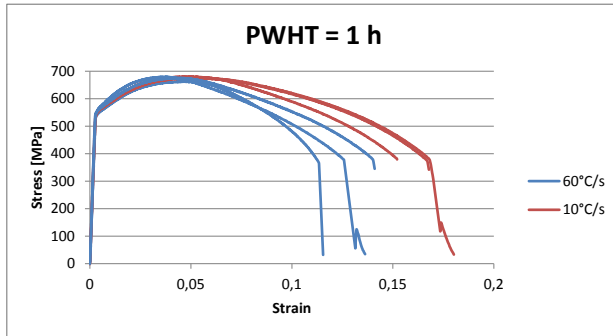
Test	Feature	Value
Hardness	Cap region	275 HV
	Root region	250 HV
Charpy impact toughness	Temperature	-20°C
	Minimum value	30 Joule
	Minimum average value	40 Joule
Tensile	Minimum yield strength	586 MPa
	Minimum tensile strength	689 MPa
	Yield to tensile ratio	0.92
	Post fracture elongation	18 %
	Minimum area reduction	35 %

Figure A.2: Abbreviations regarding tensile testing given by NS-EN 10002-1, and used in presentation of tensile results.

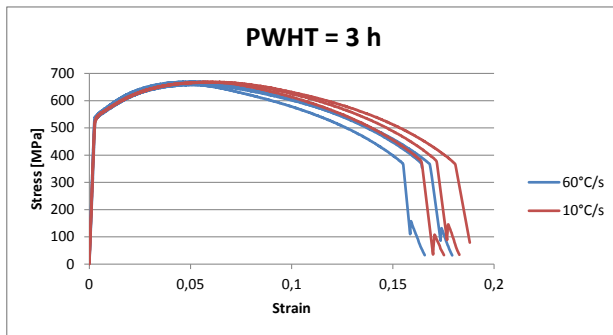
Property	Abbreviation
Original gauge length	L_0
Parallel length	L_c
Final gauge length after fracture	L_u
Force	F
Maximum force	F_m
Cross sectional area	S
Nominal strain	A
Uniform strain	A_g
Fracture strain	A_t
Elongation at F_m	A_{gt}
Percentage elongation after fracture, $\frac{L_u-L_0}{L_0} \cdot 100\%$	A^c
Percentage reduction of area, $\frac{S_0-S_u}{S_0} \cdot 100\%$	Z
Nominal stress	R
Ultimate tensile strength	R_m
0.2 % offset yield strength	$R_{p0.2}$
Modulus of elasticity	E

Figure A.3: Results from tensile testing of base material and weld simulated, but untempered material. Sample 1-3 were unaltered base material (BM). Samples 13 and 14 were weld simulated with cooling rates of 60° C/s and 10° C/s respectively. The abbreviations are according to Appendix A.2.

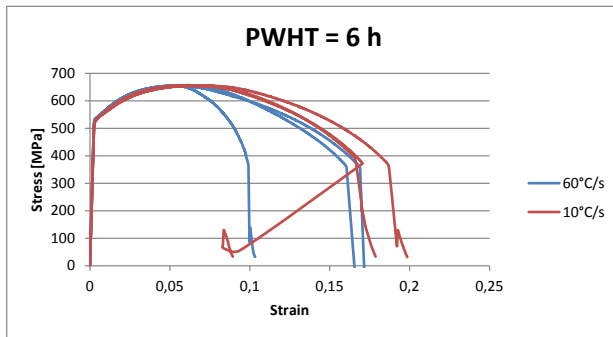
Sample	$R_{p0.2}$ [MPa]	R_m [MPa]	$R_{p0.2}/R_m$	A^c [%]	Z [%]
BM 1	551	679	0.81	17	67
BM 2	535	657	0.81	18	69
BM 3	559	676	0.83	21	69
13-1 (10° C/s)	560	671	0.83	10	68
13-2 (10° C/s)	539	652	0.83	13	68
14-1 (60° C/s)	498	617	0.81	14	69
14-2 (60° C/s)	514	635	0.81	13	69



(a)



(b)



(c)

Figure A.5: Tensile curves from testing of weld simulated and tempered material. All tempering was performed at 650°C , with varying tempering time:

a) 1 hour. b) 3 hours. c) 6 hours.

The curves in c) clearly show the problem of samples fracturing too close to the knife of the extensometer, as one curve has a disproportionate shape, and another curve show how the knife slid into the necked region at fracture, causing a reduction of the recorded strain.

Figure A.6: Results from tensile testing of weld simulated and tempered material. All samples were tempered in furnace at 650° C. The abbreviations are according to Appendix A.2.

C.R. [°C/s]	t _{temper} [h]	R _{p0.2} [MPa]	R _m [MPa]	R _{p0.2} /R _m	A ^c [%]	Z [%]
10	1	561	677	0.83	17	66
10	1	559	677	0.83	17	68
10	1	562	681	0.83	15	65
60	1	552	663	0.83	11	67
60	1	563	676	0.83	14	65
60	1	566	680	0.83	13	67
10	3	547	668	0.82	18	68
10	3	549	670	0.82	17	68
10	3	545	669	0.81	16	67
60	3	554	670	0.83	16	67
60	3	544	659	0.83	17	69
60	3	542	660	0.82	15	68
10	6	537	656	0.82	19	68
10	6	538	655	0.82	17	67
10	6	536	657	0.82	17	66
60	6	542	655	0.83	10	68
60	6	540	658	0.82	16	66
60	6	536	654	0.82	17	67

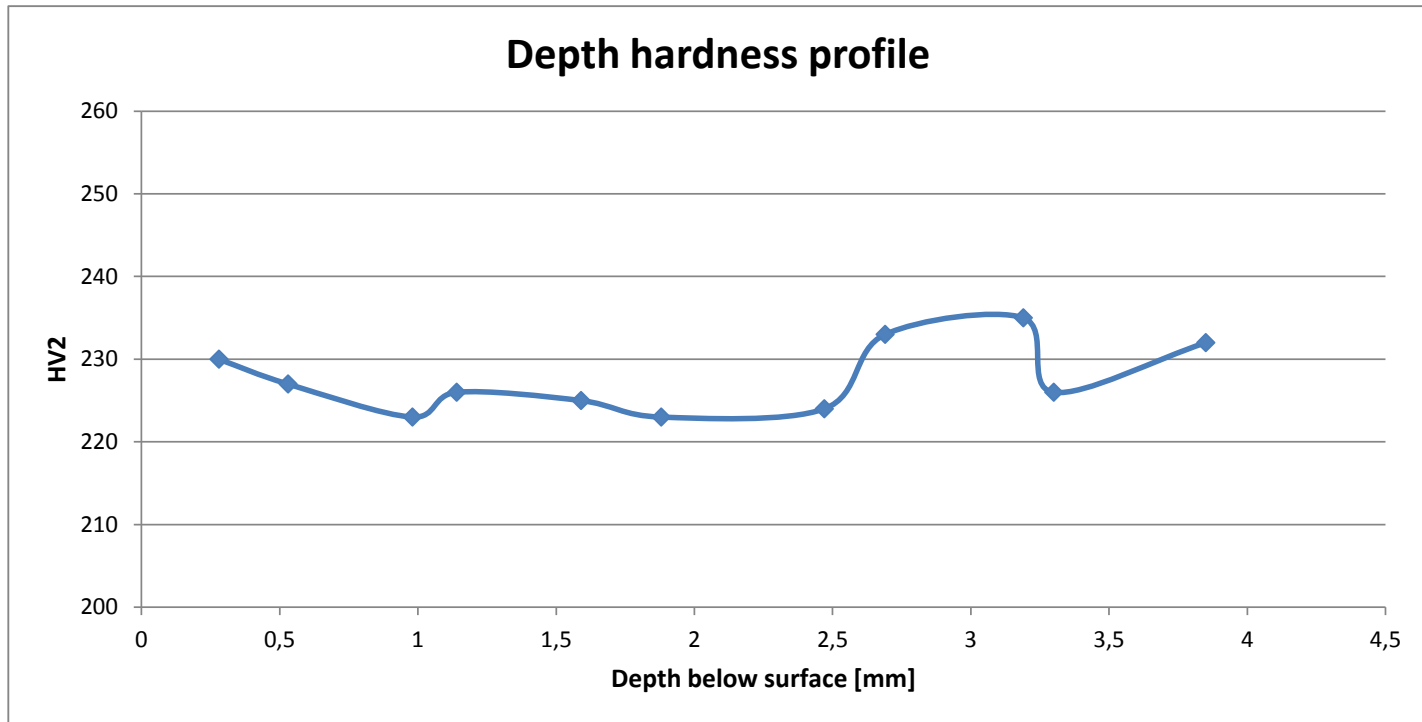


Figure A.7: *Depth hardness profile measured to ensure the reliability of the results from weld hardness measurements. Sample has been weld simulated with a cooling rate of 10° C/s and tempered for 6 hours at 625° C to provide a “worst case” scenario with regards to decarburization. No unexpected variations were observed.*

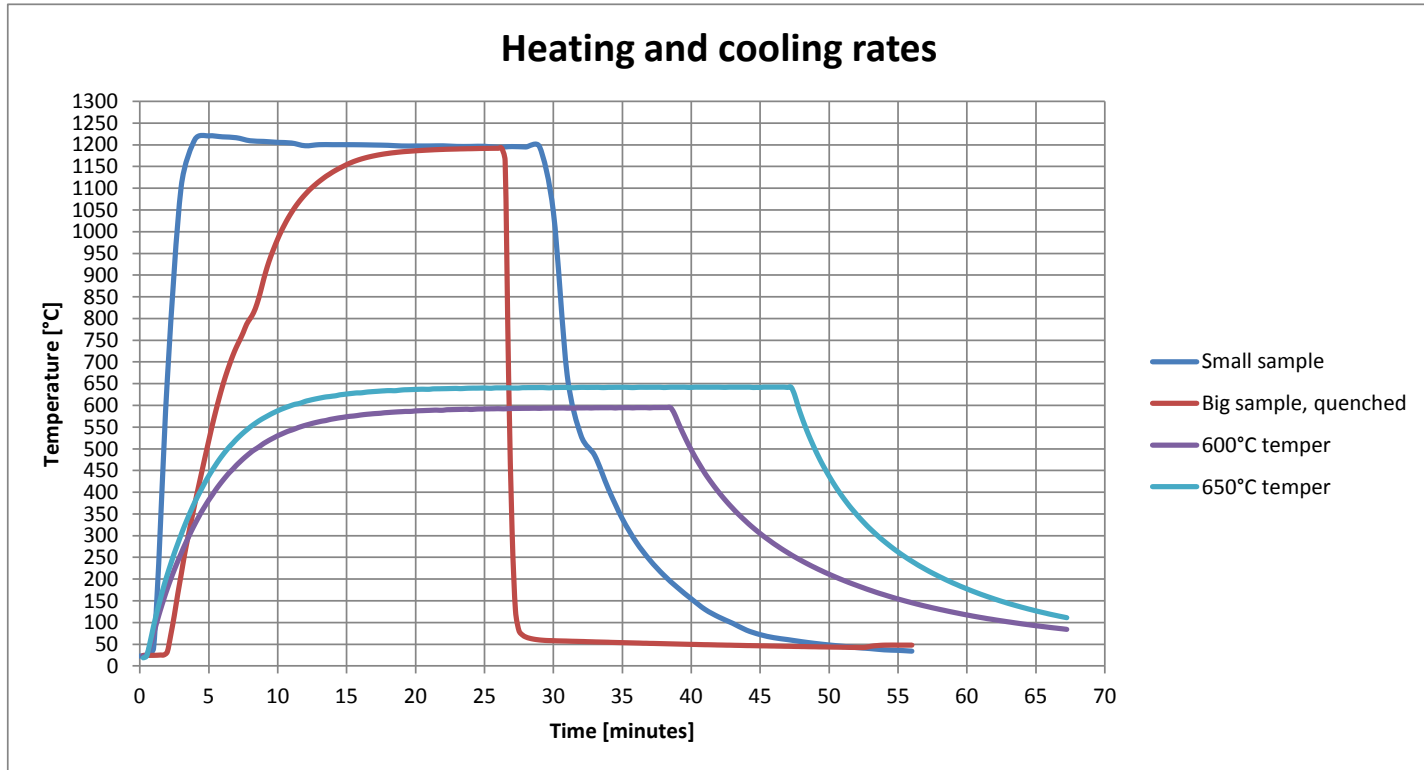
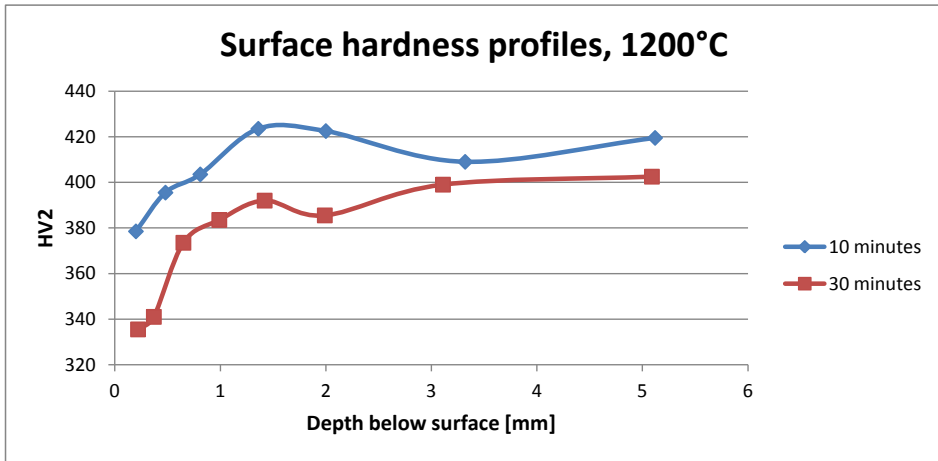
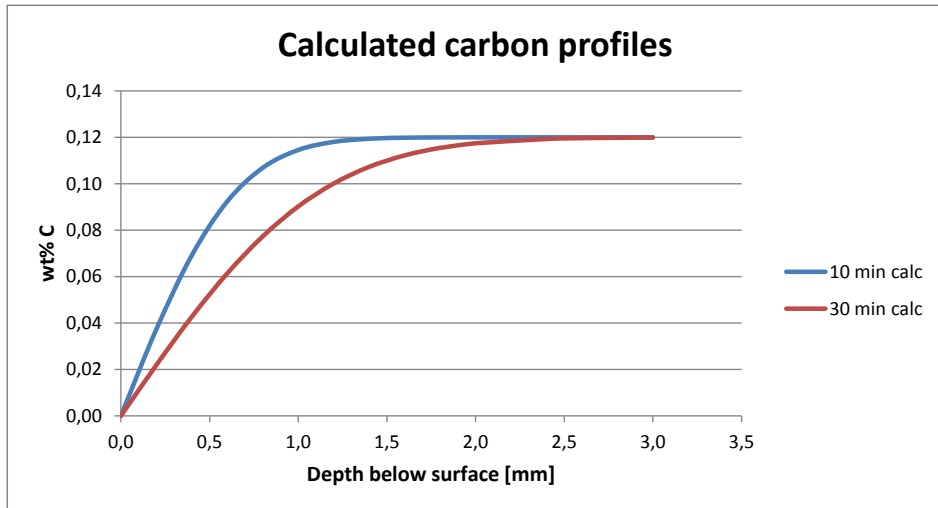


Figure A.8: Heating and cooling rates from measurements of heating rate for determination of tempering times and austenitizing time during hardening.



(a)

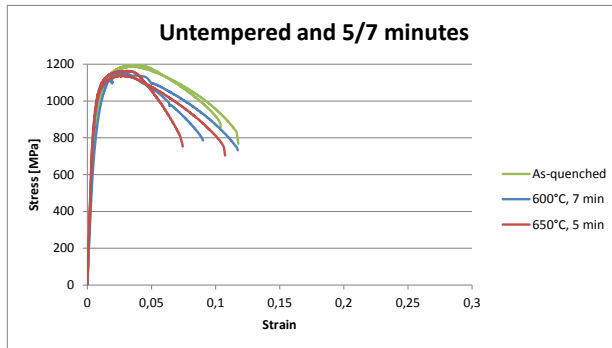


(b)

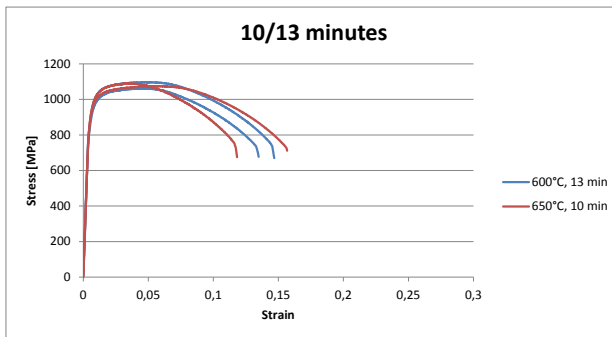
Figure A.9: Results from preliminary investigations regarding decarburization:
 a) Measured hardness profiles from samples heated to 1200°C. No substantial hardness reduction can be observed at 2 mm depth or deeper.
 b) Calculated “worst case” carbon content from holding at 1200°C for 10 and 30 minutes in carbon free environment. Simplified calculation of 1-dimensional diffusion of carbon in austenite. Can be seen that even for these calculations, the carbon content should be stable below 2 mm depth.

Figure A.10: Results from hardness measurements and tensile testing of quenched and controlled cooled material.

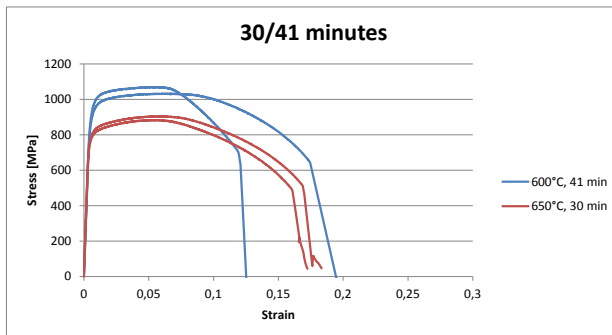
Heat treatment	HV10	R _{p0.2} [MPa]	R _m [MPa]
Q	401	918	1189
Q	398	931	1197
Q + T: 650°C, 5 min	381	957	1138
Q + T: 650°C, 5 min	387	984	1164
Q + T: 650°C, 10 min	368	946	1090
Q + T: 650°C, 10 min	364	932	1074
Q + T: 650°C, 30 min	303	794	904
Q + T: 650°C, 30 min	305	777	884
Q + T: 650°C, 1 h	271	694	781
Q + T: 650°C, 1 h	271	693	788
Q + T: 650°C, 3 h	263	666	781
Q + T: 650°C, 3 h	262	668	780
Q + T: 600°C, 7 min	382	969	1147
Q + T: 600°C, 7 min	381	874	1157
Q + T: 600°C, 13 min	367	906	1062
Q + T: 600°C, 13 min	370	943	1097
Q + T: 600°C, 41 min	358	945	1069
Q + T: 600°C, 41 min	359	904	1032
Q + T: 600°C, 15 h	261	658	749
Q + T: 600°C, 15 h	262	665	749
Q + T: 600°C, 48 h	243	614	704
Q + T: 600°C, 48 h	243	588	679
IT: 600°, 30 h	286	643	877
IT: 600°, 30 h	286	630	862
IT: 700°, 6 h	152	287	493
IT: 700°, 6 h	153	292	499
Furnace cooled	158	310	528
Furnace cooled	158	313	533



(a)

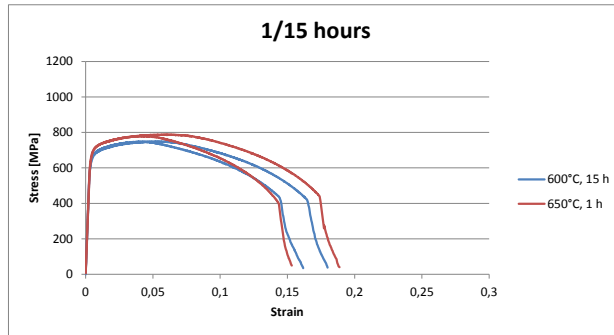


(b)

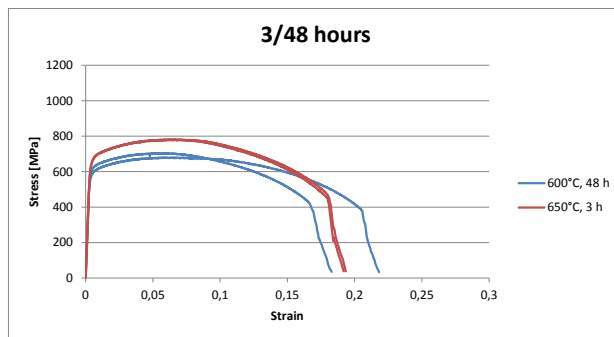


(c)

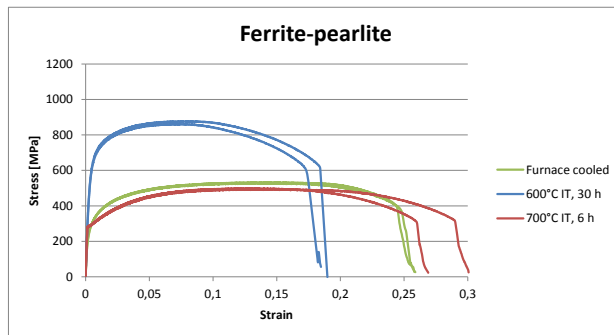
Figure A.11: Tensile curves from testing of quenched and tempered material:
 a) As-quenched material together with material tempered for 7 minutes at 600° C and 5 minutes at 650° C. Bumps in curves caused by slip in the gripping areas of the samples. Low elongation of 650° C, 5 minutes curve caused by fracture at the knife of the extensometer.
 b) Material tempered for 13 minutes at 600° C and 10 minutes at 650° C.
 c) Material tempered for 41 minutes at 600° C and 30 minutes at 650° C. Break point in 600° C, 41 minutes-curve caused by fracture at the knife of the extensometer.



(a)



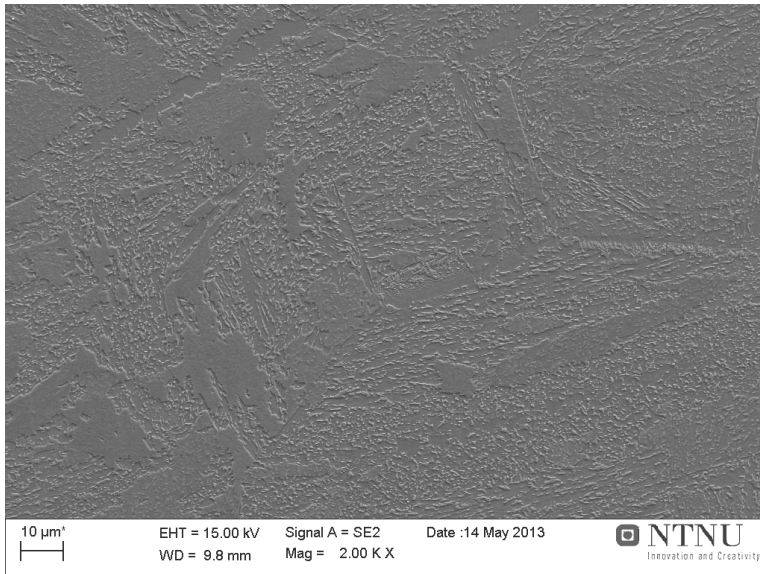
(b)



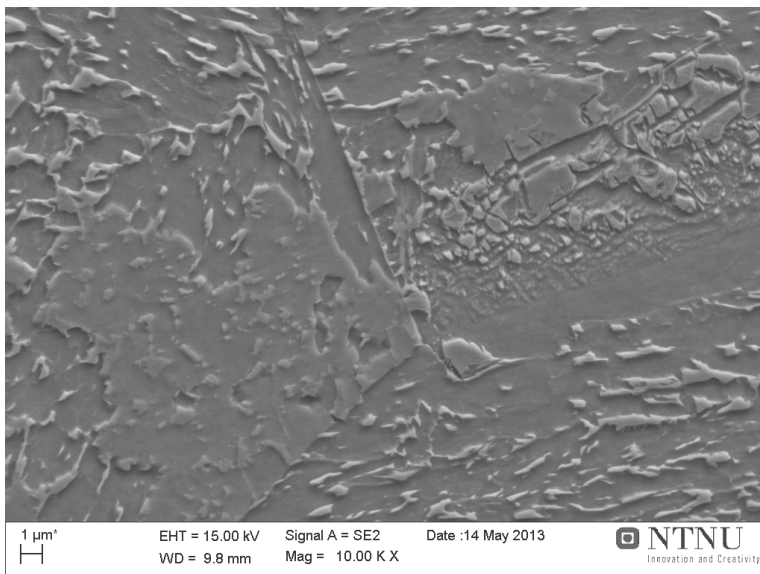
(c)

Figure A.12: Tensile curves from testing of quenched and tempered material as well as material subjected to controlled cooling:

- a) Material tempered for 15 hours at 600°C and 1 hour at 650°C .
- b) Material tempered for 48 hours at 600°C and 3 hours at 650°C .
- c) Material subjected to controlled cooling in order to produce different ferrite-pearlite microstructures. Two samples have been cooled slowly in furnace, while the four other samples were treated isothermally at 600°C and 700°C for respectively 30 hours and 6 hours.





(a)



(b)

Figure A.13: Additional SEM images of the microstructure formed during isothermal treatment at 600°C for 30 hours:

- a) Overview image. Grain boundary allotriomorph ferrite can be observed along prior austenite grain boundaries.
- b) Dissolved pearlite lamellae can be distinguished inside the grains. Less etched patches can be observed, but they seem to contain the same degenerate pearlite structure.

NTNU	Hazardous activity identification process	Prepared by	Number	Date	
		HSE section	HMSRV-26/01	01.12.2006	
HSE		Approved by	Page	Replaces	
		The Rector	1 out of 1	15.12.2003	

Unit: IMT

Date: 2013-03-18

Participants in the identification process (including their function): Trond Arne Hassel, student

Short description of the main activity/main process: Thermal weld simulation and tempering together with QT-heat treatment followed by hardness measurements and tensile testing.

Activity/process	Responsible person	Laws, regulations etc.	Existing documentation	Existing safety measures	Comment
1) Thermal weld simulation	Trond Arne Hassel	The Working Environment Act	None	Protective glasses, protective shield, deactivation switch	Training and safety instructions supplied by Sintef
2) Cutting of specimens	Trond Arne Hassel	The Working Environment Act	The HSE Handbook	Protective glasses, protective shield	
3) Metallography (including hardness measurements)	Trond Arne Hassel	The Working Environment Act	The HSE Handbook	Protective glasses, lab coats	
4) Light microscopy	Trond Arne Hassel	The Working Environment Act	The HSE Handbook		
5) Tensile testing	Pål Skaret	The Working Environment Act	The HSE Handbook		
6) QT-heat treatment	Trond Arne Hassel	The Working Environment Act	The HSE Handbook	Protective glasses, workwear, helmet with face shield, insulated gloves	

Figure A.14: Risk assessment page 1/4.

Unit: IMT

Date: 2013-03-18

Line manager: Arne Petter Ratvik

Participants in the risk assessment (including their function): Trond Arne Hassel, student

Activity from the identification process form	Potential undesirable incident/strain	Likelihood:	Consequence:			Risk value	Comments/status Suggested measures
		Likelihood (1-5)	Human (A-E)	Environment (A-E)	Economy/material (A-E)		
1) Thermal weld simulation	Touching hot metal	3	A	-	-	3A	
2) Cutting of specimens	Breakage of cutting wheel	5	A	-	A	5A	No injury obtained, cutting wheel can only break while covered by protective shield
3) Metallography (including hardness measurements)	Acid spill	4	A	-	A	4A	Strongly diluted acid results in low damage potential when protective glasses are used
4) Light microscopy	None	-	-	-	-	-	No risk of injury
5) Tensile testing	None	-	-	-	-	-	No risk of injury
6) QT-heat treatment	Touching hot surfaces or contact with steam or hot water	3	A	-	A	3A	Use protective gear, perform hardening under supervision of employee

Likelihood, e.g.:

1. Minimal
2. Low
3. Medium
4. High
5. Very high

Consequence, e.g.:

- A. Safe
- B. Relatively safe
- C. Dangerous
- D. Critical
- E. Very critical

Risk value (each one to be estimated separately):**Human = Likelihood x Human Consequence****Environmental = Likelihood x Environmental consequence****Financial/material = Likelihood x Consequence for Economy/material**

Figure A.15: Risk assessment page 2/4.

Potential undesirable incident/strain

Identify possible incidents and conditions that may lead to situations that pose a hazard to people, the environment and any materiel/equipment involved.

Criteria for the assessment of likelihood and consequence in relation to fieldwork

Each activity is assessed according to a worst-case scenario. Likelihood and consequence are to be assessed separately for each potential undesirable incident. Before starting on the quantification, the participants should agree what they understand by the assessment criteria:

Likelihood

Minimal 1	Low 2	Medium 3	High 4	Very high 5
Once every 50 years or less	Once every 10 years or less	Once a year or less	Once a month or less	Once a week

Consequence

Grading	Human	Environment	Financial/materiel
E Very critical	May produce fatality/ies	Very prolonged, non-reversible damage	Shutdown of work >1 year.
D Critical	Permanent injury, may produce serious serious health damage/sickness	Prolonged damage. Long recovery time.	Shutdown of work 0.5-1 year.
C Dangerous	Serious personal injury	Minor damage. Long recovery time	Shutdown of work < 1 month
B Relatively safe	Injury that requires medical treatment	Minor damage. Short recovery time	Shutdown of work < 1 week
A Safe	Injury that requires first aid	Insignificant damage. Short recovery time	Shutdown of work < 1 day

The unit makes its own decision as to whether opting to fill in or not consequences for economy/materiel, for example if the unit is going to use particularly valuable equipment. It is up to the individual unit to choose the assessment criteria for this column.

Risk = Likelihood x Consequence

Please calculate the risk value for "Human", "Environment" and, if chosen, "Economy/materiel", separately.

About the column "Comments/status, suggested preventative and corrective measures":


Measures can impact on both likelihood and consequences. Prioritise measures that can prevent the incident from occurring; in other words, likelihood-reducing measures are to be prioritised above greater emergency preparedness, i.e. consequence-reducing measures.

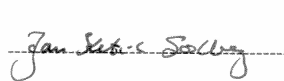
MATRIX FOR RISK ASSESSMENTS AT NTNU

CONSEQUENCE	Very critical (E)					
	Critical (D)					
	Dangerous (C)					
	Relativ. safe(B)					
	Safe(A)			1	3, 6	2
		Minimal	Low	Medium	High	Very high
		LIKELIHOOD				

Principle over accept criterion. Explanation of colors used in risk matrix.

Farge	Beskrivelse
Rød	Unacceptable risk. Action must be carried out to minimize risk.
Gul	Assessment area. Action must be evaluated.
Grønn	Acceptable risk. Action might be evaluated from other considerations.

Prepared by,


Approved by,


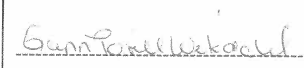
Final Approved by,


Figure A.17: Risk assessment page 4/4.